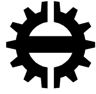

MIKA-MATTI LAURILA

SUPER INKJET PRINTED REDISTRIBUTION LAYER FOR A MEMS DEVICE

Master of Science thesis

Examiner: prof. Matti Mäntysalo
Examiner and topic approved by the Faculty Council of the Faculty of Electronics and Communications Engineering
on 04.02.2015

ABSTRACT

Laurila, Mika-Matti: Super Inkjet Printed Redistribution Layer for a MEMS Device
Tampere University of Technology
Master of Science Thesis, 73 pages, 6 Appendix pages
December 2015
Master's Degree Programme in Electrical Engineering
Major: Electronics
Examiner: Adj. Professor Matti Mäntysalo
Keywords: Electronics miniaturization, microelectronics packaging, printed electronics, redistribution layer, electrohydrodynamic inkjet printer

Printed electronics (PE) is a novel area of electronics manufacturing where functional inks and suitable ink deposition devices, such as inkjet or roll-to-roll equipment, are used to create electrically functional features. A lion's share of current applications are in the field of low-cost, large-area electronics where the printing technologies have a significant advantage over the conventional methods due to faster processing speed and higher process flexibility. Since this has been seen as the holy grail of printed electronics, little research has been done on the field of small-area applications such as microelectronics packaging. However, with recent developments in high resolution printing, this application area should be within the reach of printing technologies as well.

The main purpose of this study is to find out if the production methods developed for printed electronics could be used in the packaging of microelectromechanical systems (MEMS). Specifically, the aim is to print a high density redistribution layer (RDL) of a MEMS device package with a state of the art electrohydrodynamic (EHD) inkjet printer. By using inkjet technology instead of the current method, electrochemical plating, the costs and environmental impact of the fabrication process could be reduced significantly. This is based on the fact that inkjet printing is an additive and electrochemical plating a subtractive manufacturing method. Subtracting material leads to larger amount of wasted resources and additionally, the chemicals used to etch the copper plating are environmentally unfriendly. Additive nature of the inkjet technology increases the flexibility of production process by making the prototyping easier and enabling shorter exchange-of-die times. Applicability of EHD printing in RDL manufacturing is demonstrated by printing high density interdigital and meander structures.

The secondary purpose of the thesis is to gain knowledge about operation of an EHD printer. Since this is a new development in the field of printed electronics, the existing literature is quite limited. Therefore, in addition to short literature study, statistical tools are used to look for significant parameters affecting the printing process. This analysis results in statistical models which relate the printing parameters to conductor width, thickness and sheet resistance.

TIIVISTELMÄ

Laurila, Mika-Matti: Super Inkjet Printed Redistribution Layer for a MEMS Device
Tampereen Teknillinen Yliopisto
Diplomityö, 73 sivua, 6 liitesivua
Joulukuu 2015
Sähkötekniikan diplomi-insinöörin tutkinto-ohjelma
Pääaine: Elektroniikka
Tarkastaja: Dosentti Matti Mäntysalo
Avainsanat: Elektroniikan miniaturisaatio, mikroelektroniikan pakkaus, painettava elektroniikka, redistribution-kerros, elektrohydrodynaaminen mustesuihkutulostin

Painettava elektroniikka on suhteellisen uusi elektroniikan valmistusmenetelmä, jossa valmistetaan funktionaalisia musteita ja yhteensopivia painomenetelmiä hyväksi käyttäen sähköisiä rakenteita. Tällä hetkellä kyseisiä valmistusmenetelmiä käytetään pääasiassa halpojen, suuren pinta-alan omaavien rakenteiden tekemiseen sillä nämä käyttökohteet hyötyvät merkittävästi painoprosessin nopeudesta ja joustavuudesta. Tästä johtuva painotekniikan kilpailuetu on merkinnyt myös sitä, että sellaiset potentiaaliset käyttökohteet, joissa kilpailuetu ei ole yhtä selkeä, ovat jääneet vähemmälle huomiolle; esimerkkinä tästä pienten sähköisten rakenteiden painaminen mikroelektroniikan pakkauksiin.

Tutkielman päätarkoituksena on siis selvittää voidaanko painettavassa elektroniikassa käytettäviä valmistusmenetelmiä soveltaa mikroelektromekaanisen systeemin (MEMS) pakkauksessa. Tarkalleen ottaen tutkimus koskee mahdollisuutta painaa MEMS pakkauksen signaalijakeluun käytettävän kerroksen (RDL) johtimet elektrohydrodynaamisella (EHD) mustesuihkutulostimella. Käyttämällä mustesuihkutulostusta nykyisen valmistusmenetelmän sijaan voidaan vähentää materiaalikustannuksia, lyhentää valmistukseen kuluvaa aikaa sekä parantaa tuotannon ympäristöystävällisyyttä. Saavutettavat edut perustuvat siihen että nykyinen valmistusmenetelmä, elektrokemiallinen pinnoittaminen, on luonteeltaan subtraktiivinen toisin kuin mustesuihkutulostus; jälkimmäisessä ainoastaan musteessa käytettävä liuotin ja nanopartikkelien stabilointiin käytettävät polymeerit ovat hukkamateriaalia. Ympäristön kannalta merkittävää on myös materiaalin poistamiseen käytettävien haitallisten happojen välttäminen. Lisäksi mustesuihkutulostuksen digitaalisuus parantaa tuotannon joustavuutta ja helpottaa esimerkiksi prototyyppien valmistusta. EHD tulostimen soveltuvuutta RDL:n valmistuksessa demonstroidaan painamalla tiheitä johdinrakenteita, joissa johdinten leveys ja välimatka on noin viisi mikrometriä.

Tämän lisäksi tutkielman tarkoituksena on selvittää EHD tulostimen sielunelämää. Koska kyseessä on uusi mustesuihkutulostinteknologia, siihen liittyvien tieteellisten julkaisujen määrä on rajallinen. Tästä syystä laitteen toimintaa yritetään selvittää kirjallisuusselvityksen lisäksi tilastollisin menetelmin. Analyysin tuloksena on tilastollinen

malli, joka kertoo johdinleveyden, -paksuuden ja -resistanssin tulostusparametrien funktiona.

PREFACE

The work for this thesis was done in the Department of Electronics and Communications Engineering at Tampere University of Technology. The work is supported by ENIAC-JU Project Prominent grant No. 324189 and Tekes grant No. 40336/12.

I would like to thank my examiner and instructor Adj. Professor Matti Mäntysalo for providing the resources and necessary guidance for this work. I would also like to thank my co-workers Behnam Khorramdel, M.Sc., Ayat Soltani, M.Sc., Tiina Vuorinen, M. Sc., Juha Niittynen Ph.D., Jari Suikkola, M. Sc., and Lydia Seppälä B. Sc. for enlightening conversations and support during the work.

I would also like to thank my family and friends for their support during my studies.

Tampere, Finland

Mika-Matti Laurila

CONTENTS

1. INTRODUCTION ... 1
2. MICROELECTRONICS PACKAGING ... 3
 2.1 Evolution of system level packaging technologies ... 4
 2.2 System-in-Package (SiP) ... 5
  2.2.1 Interposer ... 6
  2.2.2 Redistribution layer (RDL) ... 7
  2.2.3 Manufacturing process for printed RDL ... 9
  2.2.4 Through silicon via (TSV) ... 11
 2.3 Wafer level packaging (WLP) ... 13
3. INKJET PRINTED ELECTRONICS ... 15
 3.1 Inks ... 15
  3.1.1 Conductive nanoparticle inks ... 16
  3.1.2 UV-curable dielectric inks ... 18
 3.2 Conventional inkjet technologies ... 18
  3.2.1 Continuous inkjet (CIJ) ... 19
  3.2.2 Drop-on-demand (DoD) inkjets ... 20
 3.3 Super Inkjet (SIJ) ... 21
  3.3.1 Machinery ... 21
  3.3.2 Operating principle ... 22
  3.3.3 Suitable parameter values ... 25
  3.3.4 Operating the equipment ... 27
 3.4 Conventional DoD printers vs. SIJ ... 28
4. SIJ PROCESS OPTIMIZATION ... 30
 4.1 Suitable inks ... 30
  4.1.1 Test for ink stability ... 31
  4.1.2 Stability test results ... 32
  4.1.3 Conclusion ... 34
 4.2 Conductor width ... 35
  4.2.1 Significant parameters ... 35
  4.2.2 Response surface model for parameters effects ... 38
 4.3 Conductor topography and resistance ... 43
  4.3.1 Topography ... 44
  4.3.2 Resistance ... 51
5. RDL DEMONSTRATORS ... 56
 5.1 Designs ... 56
 5.2 Demonstrators ... 57
6. CONCLUSIONS AND FUTURE WORK ... 60
REFERENCES ... 62
APPENDIX A ... 65

APPENDIX B..68

APPENDIX A: Factorial DoE for conductor width

APPENDIX B: Response surface DoE for conductor width

LIST OF ABBREVIATIONS

AD	Anderson-Darling statistic
Adj. MS	Adjusted mean of squares
Adj. SS	Adjusted sum of squares
Ag	Silver
Al	Aluminum
AFM	Atomic force microscope
ANOVA	Analysis of variance
Au	Gold
CIJ	Continuous inkjet
CL	Confidence limit
CPU	Central processing unit
CVD	Chemical vapor deposition
Cu	Copper
DF	Degrees of freedom
DoD	Drop-on-demand
DOE	Design of experiments
DRAM	Dynamic random access memory
DRIE	Deep reactive ion etching
EHD	Electrohydrodynamic
F-value	Ratio of mean of squares
H2O2	Hydrogen peroxide
IC	Integrated circuit
I/O	Input/output
MCM	Multichip module
MEMS	Microelectromechanical system
N	Sample count
Ni	Nickel
P-value	Statistic used for testing a statistical hypothesis
PVD	Physical vapor deposition
PWB	Printed wiring board
RDL	Redistribution layer
Si	Silicon
SIJ	Super inkjet
SiO2	Silicon dioxide
SiP	System-in-package
SoB	System-on-board
SoC	System-on-chip
SoP	System-on-package
StDev	Standard deviation
Ti/W	Titanium/tungsten
TSV	Through silicon via
UV	Ultraviolet
WF	Waveform
WLP	Wafer level package

LIST OF SYMBOLS

Symbol	Description
d	Nozzle diameter
$\boldsymbol{E}$	Electric field
e	Base of natural logarithm
ϵ_0	Dielectric constant of vacuum
ε	Permittivity
$\boldsymbol{F}$	Force field
f	Frequency
h	Distance between nozzle tip and substrate
h_{p-v}	Peak-to-valley height
k	Nozzle form factor
k_e	Coulomb's constant
L	Length
λ	Lambda value returned by Box-Cox procedure
p	Nozzle curvature
P_e	Electrostatic pressure
P_s	Surface tension pressure
P_e	Electrostatic pressure
q	Unit charge
r_d	Droplet radius
R	Resistance
R_{sheet}	Sheet resistance
σ	Conductivity of ink
t	Thickness
τ	Dielectric relaxation time
V	Voltage between nozzle and substrate
v	Printing speed
V_{bias}	Bias voltage between nozzle and substrate
V_{max}	Amplitude of voltage between nozzle and substrate
w	Width
$wt\boldsymbol{\%}$	Weight percent
X_o	Original data point value
X_t	Transformed data point value
γ	Surface tension

.

1. INTRODUCTION

In recent years electronics industry has made rapid advancement on two fronts, microelectromechanical systems (MEMS) and printed electronics. MEMS are micrometer scale miniature devices which include electrical circuits, such as semiconductor chips, acting as information processing units, and mechanical sensors or actuators acting as information inputs or outputs. The applications of MEMS devices are many including pressure sensors, accelerometers, gyroscopes and microengines. The various application possibilities have led to a rapid growth of the MEMS market and opened up lucrative business opportunities for electronics manufacturers. As more operators have flooded the market, the competition between them has become more intense. Reducing manufacturing costs is one of the main ways to maintain the competitive edge. Major cost reductions can be done for example on device or package level. Here the focus will be on the latter. [1]

Printed electronics is a novel area of electronics still seeking its breakthrough application. The basic idea is to print functional materials, such as conductive or semiconductive inks, on a chosen substrate. The choice of substrate depends on the printing method, which are similar to those used in graphic industries: inkjet, offset lithography, flexography, gravure and screen printing. All these methods are additive, meaning that they only add material to substrate instead of taking it away. This is advantageous since material costs are decreased as is the negative impact on environment. However, only the inkjet technology allows for both flexible and rigid substrates; it also enables processing of substrates with 3D surface topography. [2, 3]

In MEMS package fabrication, conductors connecting the device to package are usually made by electroplating copper or gold on a substrate and then etching it away from the parts where it is unwanted. By substituting this subtractive process step by an additive method, such as inkjet printing, manufacturing costs could be significantly reduced. Considering all printed electronics fabrication methods, inkjet seems to be most suitable for this purpose since it offers necessary process flexibility and high enough resolution. The latter has been made possible by a very recent development in inkjet technology: Super Inkjet (SIJ) printer invented by K. Murata et al. The SIJ is an electrohydrodynamic (EHD) printer capable of sub-femtoliter droplets [4]. This enables line widths in micrometer range; almost an order of magnitude smaller than conventional piezo- or heat actuator based inkjet technologies. [2, 3]

Thus, the objective of this thesis is to find out if the SIJ could be used in fabrication of a certain part of MEMS package, the redistribution layer (RDL). In order to show that this

is indeed possible, statistical models are generated for conductor width, thickness and sheet resistance; demonstrators with high density conductor structures will be printed as well. Content of the thesis is following:

Chapter two describes microelectronics packaging in general with emphasis on the RDL. It also points out other parts of microelectronics packaging which could be implemented using inkjet technologies.

Chapter three is used to familiarize the reader with printed electronics fabrication technologies with emphasis on conventional drop-on-demand printers and the SIJ. It also contains information about the relevant functional inks.

In chapter four SIJ printed conductors are examined using atomic force microscopy and four point resistance measurements. Statistical tools are used to generate models for conductor width, thickness and resistance.

Chapter five shows two single layer high-density RDL demonstrators with five micron conductor width and spacing. This is followed by chapter six which summarizes the thesis and also makes some remarks about future work regarding multilayer RDLs.

2. MICROELECTRONICS PACKAGING

Microelectromechanical systems (MEMS) are very small electromechanical devices which function either as actuators or sensors. Sensor type MEMS include various pressure sensors, accelerometers and gyroscopes, whereas actuator type MEMS are well represented by the piezoelectric pressure generators. The former can be found for example in cars and airplanes, whereas the latter are necessary for droplet generation in drop-on-demand inkjet printers. Since the MEMSs are also microelectronic devices, they share many common traits with the ICs; these regard the material choices, manufacturing methods and packaging approaches. [1, 5]

The basic function of any microelectronics package is to protect the device from the environment, enable electrical and mechanical connections to the outside world and dissipate heat generated by the device. The focus of package engineering depends on the nature of the device itself. Most of the IC packaging focuses on efficient thermal management, hermetic sealing and very fast electrical interconnects, whereas the focus of MEMS device packaging varies heavily depending on application area. In some cases mechanical durability and thermal management are the main focus, since the MEMS have to remain operational in harsh environments. In other cases the package has to enable sufficient interaction between the environment and device, but at the same time protect the device from environmental extremities; one example of this is the pressure sensor in which the package has to allow the measured medium to interact with the measurement device without compromising device integrity. In conclusion, the MEMS package engineering must be more flexible compared to IC package engineering since most IC's are alike, but MEMS are not. [5, 6]

Although package engineering focus may vary between the different types of MEMS devices, the system level packaging approaches of MEMS are inherited from other microelectronics devices. All in all five major system level technologies exist in microelectronics packaging: system-on-board (SoB), multichip module (MCM), system-on-chip (SoC), system-in-package (SiP) and system-on-package (SoP). Future trend in system level MEMS packaging seems to be towards higher three dimensional integration with SiP architecture. Other packaging technologies will be discussed shortly in chapter 2.1 followed by a more detailed discussion regarding the SiP in chapter 2.2. [5, 6]

In addition system level packaging, the MEMS require protection on device level as well. In this case the classification of packaging technologies can be done based on whether the individual devices are packaged before or after they are cut from the wafer.

The current trend in MEMS is towards the latter option i.e. wafer level packaging (WLP). This will be discussed shortly in chapter 2.3.

2.1 Evolution of system level packaging technologies

Main driver behind evolution of system level packaging technology has been the need to integrate more functionality in a single package. This need has been created by the decreasing size of electronics devices (mobile phones etc.), and increasingly complex functions the devices have to perform (multitasking, GPS, RF etc.). In practice, the integration is achieved either by incorporating chips of different functionalities in a single package (MCM, SiP and SoP) or by integrating multiple functionalities on a single chip (SoC). [5, 6]

As shown in Figure 1 until the late 70s the only package option was the System-on-Board (SoB) which consisted of discrete components connected to a system board. This was strictly a 2D type of integration where the size reduction was achieved by decreasing interconnection pitch and wiring dimensions – that is, by making the components smaller. The MCM was the next step on the evolutionary path towards 3D integration. Although still strictly 2D, the MCM contained a feature which would later find use in 3D SiP and SoP solutions: the functionalities of the SoB discrete components were incorporated in a *single package* as interconnected chips. [5, 6]

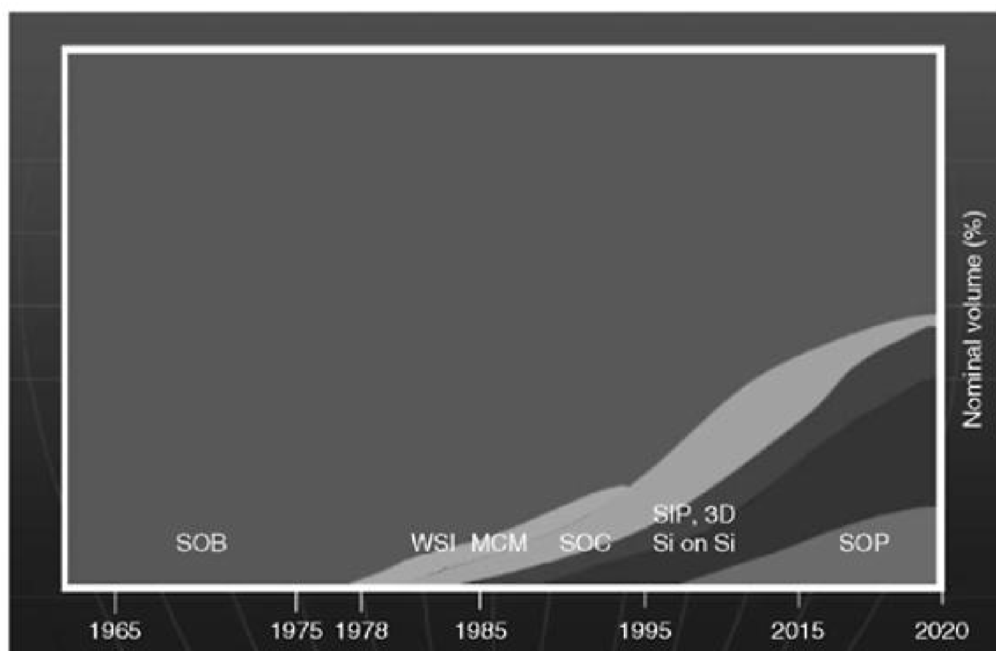

Figure 1: *Evolution of electronics packaging. [6]*

The SoC took the 2D integration a step further by incorporating the different functionalities on a single chip made of single silicon wafer. This proved to be handy in IC applications, but problematic in case of MEMS devices due to limitations created by the SoC structure: the doped silicon wafer used for the active components, such as transistors, cannot be used for creating micromechanical features. On top of this, the SoC integration is only cost effective when batch size is very large. These requirements can be easily met in IC industry, but in MEMS industry they lead to SiP as the best option for enhancing the integration. [5, 6]

2.2 System-in-Package (SiP)

The SiP consists of stacked chips with each chip executing a specific function. Since the chips can be now manufactured from the most suitable substrate material, cost benefits of integration become apparent already at smaller batch sizes. The other major advantage of the SiP over SoC is the 3D nature of the packaging: since the chips are stacked on top of each other, footprint of the package can be reduced and electrical interconnects between chips will be shorter. This reduces the electrical losses. [5, 6]

The SiP can be implemented with wire or flip chip bonding. In the first case, electrical connections from the chip I/O's to the interposer are done with thin leads or wires. It is also possible to connect the bottommost chip with flip-chip bonds and other chips with wire bonding to reduce some of the signal propagation losses which take place in the wires. A further step is to replace the wire bonds with flip-chip bonds between all the chips. The I/O count will still be quite limited, but the signal propagation losses reduce significantly. [5, 6]

The ultimate goal of SiP packaging is to create electrical connections using metal plated holes which are drilled through chip or interposer silicon – a so called through silicon via (TSV) technology. In this case, connection between subsequent chips is made simply by connecting the designated TSVs with conductors. Similar to flip-chip bonding of all the chips, this approach reduces the signal propagation losses to minimum. However, it also allows for smaller, chip-scale interposer to be used. As a result, a true chip-scale package will be formed. [5, 6]

A simplified TSV SiP package containing multiple functionalities is shown in Figure 2. In real life SiP, the number of vias is much higher and connections are made between the chips as well as between the chip and the interposer. However, even from the above figure it is apparent that this approach enables higher interconnection density. In addition, signal propagation losses will decrease due to shorter interconnection length and package size will be reduced as a consequence of getting rid of space demanding wire bonds. [5, 6]

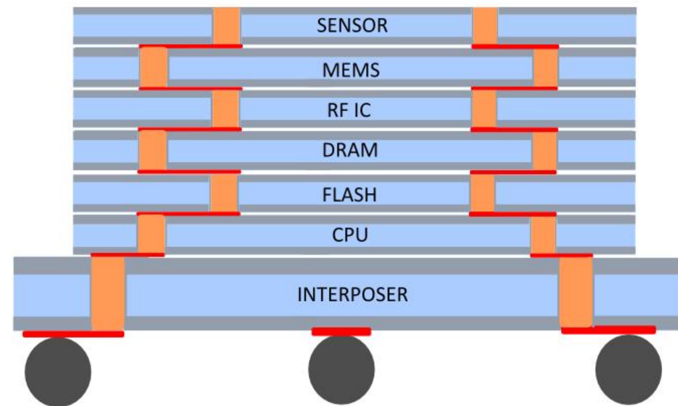

Figure 2: *TSV connected (simplified) SiP containing multiple functionalities. The TSVs are marked with brown and RDL conductors with red. In reality, each chip contains multiple TSVs to enable signal transfer between chips as well as the environment.*

In addition to chips themselves, a key component of SiP is the interposer. It acts as an I/O space transformer enabling the high pitch I/O's of the chip to be connected to the low pitch I/O printed wiring board (PWB). [5]

2.2.1 Interposer

Power, signal and ground connections can't be made directly between the PWB and the bottommost chip of SiP. The limiting factor is the difference between chips micron scale I/O pitch and PWBs minimum pitch of tens of microns. To conform the electrical connections from chip to substrate, an interposer ("chip carrier") is needed. Since the chip I/O count may be in hundreds, resulting interposer needs to be multilayered. This kind of structure is achieved by using TSVs which are electrically connected by redistribution layers (RDLs). The Figure 3 shows a simplified multilayer interposer. [5, 6]

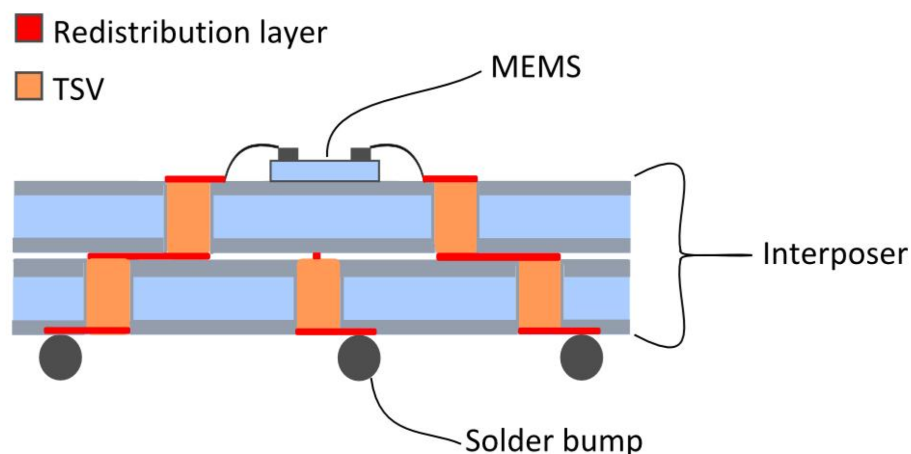

Figure 3: *Multilayered interposer. The connected device could as well be a stack of chips of different functionalities as shown in previous figure.*

Depending on the chip I/O pitch, RDL may need to have high density. This translates to conductor widths of under 10 microns and similar conductor-to-conductor distances. Since the RDLs and TSVs are important parts of signal redistribution process, they deserve their own sub-chapters. [5, 6]

2.2.2 Redistribution layer (RDL)

Redistribution layers (RDLs) play a major role in rerouting signal and power paths. They make the electrical connections between bonding pads of package and designated TSVs; between designated TSVs of different layers; and between designated TSVs of interposer and chip I/O bumps. Figure 4 shows a schematic of a redistribution layer between interposer TSVs and I/O bonding pads. [5, 6]

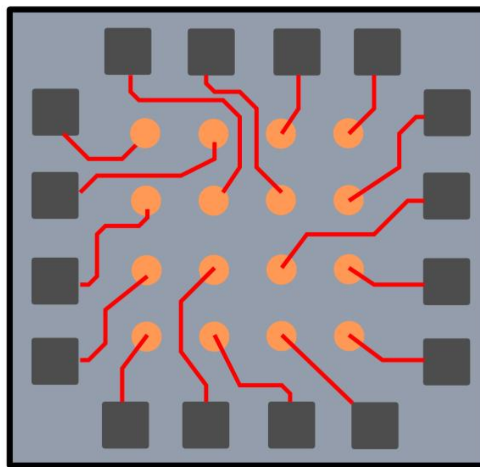

Figure 4: *Schematic of redistribution layer between TSVs and bonding pads.*

In a sense, manufacturing RDL layers is first and foremost a question of finding suitable materials. The MEMS are usually manufactured on glass or, as in the case of this study, a silicon substrate. The latter requires a passivation layer on the surface because of the semiconducting nature of the base material. Passivation layer can be a micro coating of nitride or oxide; for example in case of silicon, silicon oxide is a common choice. This also protects the bulk from environmental contaminants. The conductor material is usually gold (Au), copper (Cu) or aluminum (Al). Depending on the choice of conductor material, additional material layer may be added to improve its adhesion to the substrate. This layer may also act as diffusion barrier to prevent movement of metal atoms from conductors to semiconducting bulk. If the diffusion barrier is conductive, it has to be removed between the conductors by suitable etchant. [5, 6]

With such a variety of different materials, it is clear that the conventional manufacturing process must be quite complicated. Process steps for RDL electroplating are shown in Figure 5.

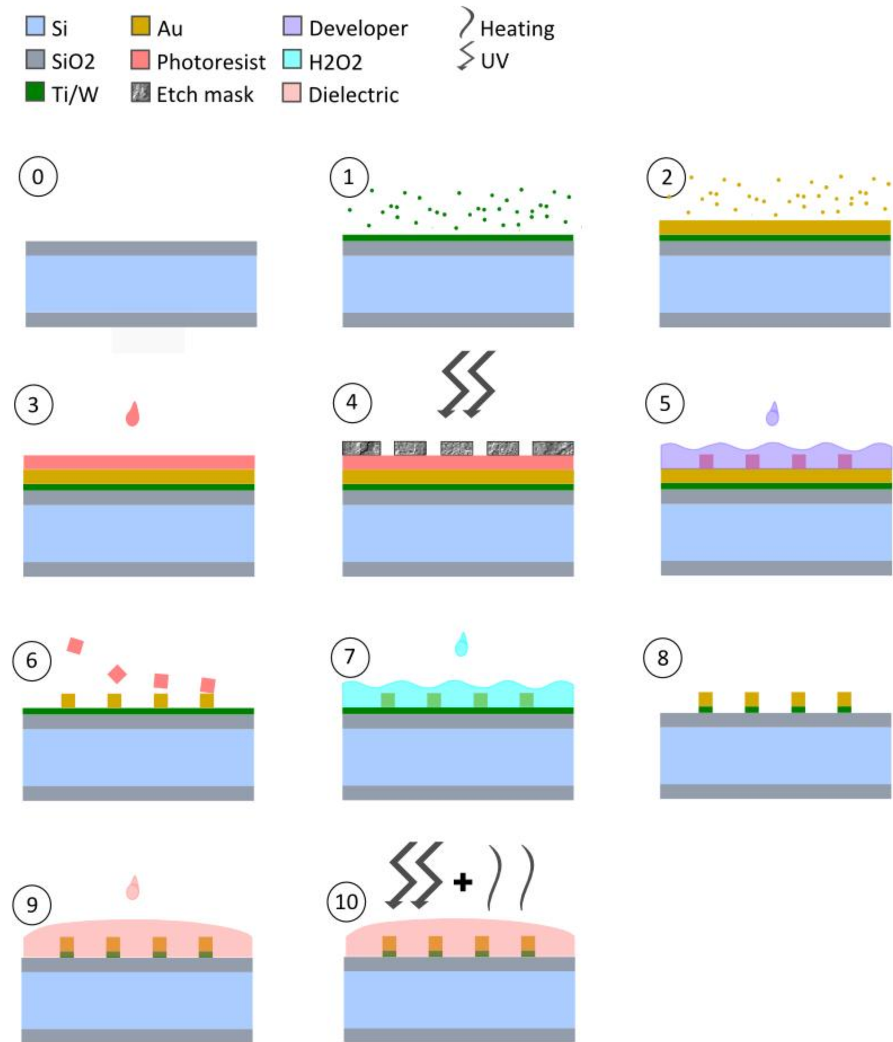

Figure 5: *Conventional RDL manufacturing process: 1) Ti/W sputtering; 2) Au electroplating; 3) photoresist deposition; 4) masking and UV-curing; 5) Au etching; 6) removing photoresist; 7) Ti/W etching; 8) conductors ready; 9) dielectric deposition and 10) UV-curing and hard baking the dielectric layer.*

In the example above, Au is used as conductor material. The process starts when a thin layer of titanium tungsten (Ti/W) is first sputtered on top of silicon oxide (SiO2) passivation layer. Purpose of the Ti/W is to improve adhesion of gold to the substrate and act as a diffusion barrier. In second step, Au layer is deposited on top of the Ti/W by electroplating. The plating thickness determines the resulting conductor thickness. In third step, a photoresist is added on top of the Au. Since the resist in this example is positive, the masking is done so that the areas exposed to UV-light align with the conductor pattern (step four). After exposing the pattern, the unexposed photoresist is removed. In fifth step the bare Au is removed by suitable developer (etchant). After removing rest of the photoresist in the sixth step, Ti/W adhesion promoter must be removed between the conductors. For this purpose hydrogen peroxide (H2O2) is used. In

this case the last steps are depositing and curing of dielectric on top of the conductors. [5, 6, 7]

The conventional manufacturing method has some built-in challenges. Even in high-density RDLs the area to be etched is likely over fifty percent of metallized surface area. The photoresist and etchants also add to the amount of waste material. Additional environmental concerns are created by the latter, which may be toxic themselves or create toxic compounds with the etched metal. So far, the benefits of the method have outweighed its drawbacks. For example the conductor dimensions can be reduced to micrometer range, fulfilling the requirements of high density RDL. This also means that the conductor edges should be well defined (i.e. straight without scalloping), thereby reducing the parasitic losses in conductors. Theoretically, the conductivity of metal traces formed by the lithographic process should be almost that of the bulk metal; for example, electroless plating of copper conductors on palladium precursor resulted in conductivity of 77% bulk conductivity [8]. Compared to inkjet printed conductors with conductivity approximately 50% of bulk, the value is somewhat higher [9]. [5, 6]

The literature on the actual electrical characteristics of the ideal high density RDL is very scarce. For the current project the goal parameters are given in Table 1.

Table 1*: *Design parameters for high density RDL. [5, 6]

Parameter	Value
Material	Cu, Al or Au
Conductor width	< 10 micron
Conductor thickness	1 to 2 micron
Sheet resistance	minimal

2.2.3 Manufacturing process for printed RDL

In order to be able to compare the conventional RDL manufacturing process with the proposed inkjet process, the latter is presented here. Figure 6 contains the steps from sputtering the silicon wafer with titanium tungsten (Ti/W) to curing and hard baking the dielectric layer.

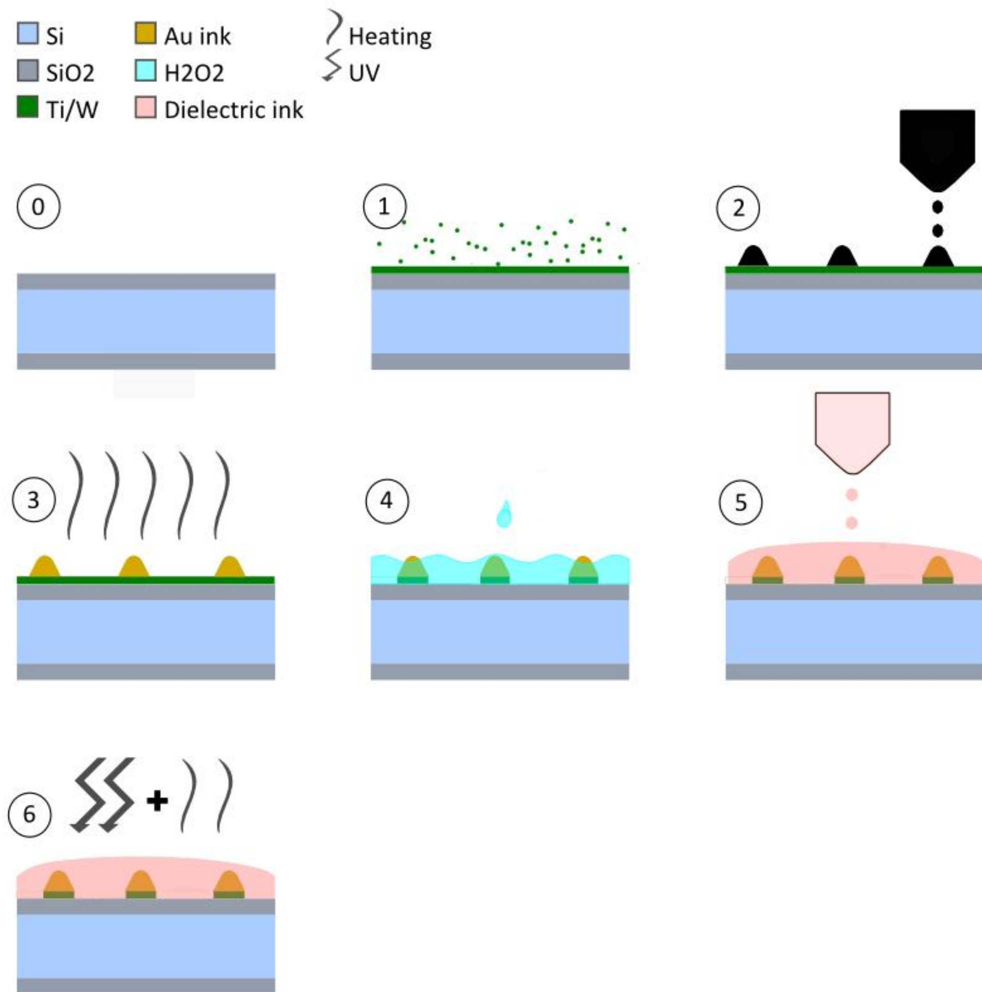

Figure 6: *RDL printing process: 1) Ti/W sputtering; 2) depositing Au-nanoparticle ink; 3) sintering the ink; 4) Ti/W etching; 5) depositing dielectric; 6) UV-curing and hard baking the dielectric layer.*

The blank wafer has one to two micron SiO2 layers on back and front. The purpose of the SiO2 is to prevent the electrical connection between the conductors and the pure silicon. A thin layer of Ti/W is then deposited on top of the front SiO2. Similar to conventional fabrication method, it acts as a diffusion barrier and improves the adhesion between the conductive material and the substrate. After Ti/W deposition the substrate is cleaned properly; in this case wiping with isopropanol followed by oxygen plasma treatment. The nanoparticle ink, in this case Au, is then deposited using the SIJ. After depositing the wet ink on the substrate, the wafer is sintered. The sintering time and temperature depend on the conductive material; for gold inks the parameters vary from 30 to 60 minutes and 200°C to 300°C. Purpose of this step is to evaporate solvent; break up polymer coating on top of the nanoparticles and induce diffusion. The result will be formation of conductive traces. In the following step, the Ti/W diffusion barrier between the conductors is removed in order to prevent short circuiting the structure; this is done with H2O2 wet etching. The etchant must be such that it does not etch the conductive material; for example Ag inks require different etchants compared to Au or Ni. Af-

ter etching the Ti/W, dielectric ink is deposited on top of the conductors. This can be done with either the SIJ or even the conventional piezo-based printer if the structure is large enough. For this example a UV-curable dielectric ink is used where the cross linking of the polymers is induced by UV-light. The hard baking phase is done in order to get rid of the remaining solvent and increase the chemical, structural and thermal stability of the layer.

The process steps two and three can be repeated on top of the dielectric layer to create a multilayer structure with two conductive layers separated with dielectric. Major cost saving potential of this type of process lies within the process steps two and five. However, the savings potential relate mostly to material, not necessarily the process time. As will be shown in chapter 4, reducing the conductor resistance to desirable values necessitates printing of multiple layers, thus increasing the process time. Furthermore, it is difficult to predict if, in future, it will become possible to use multiple print heads (nozzles) in an EHD printer setup to reduce the process time. Before this happens, the process times of the two manufacturing methods can't be compared sensibly.

2.2.4 Through silicon via (TSV)

TSVs or through silicon vias are the other important technology enabling signal redistribution in interposers. Manufacturing of TSVs requires optimization between different material choices; also the materials deposition techniques affect the yield and throughput. [6]

The TSVs can be drilled through the silicon interposer with various methods: laser drilling; deep reactive ion etching (DRIE) with cryogenic or Bosch process; and anisotropic or isotropic wet etching. The inner surfaces are passivated in order to prevent the silicon from conducting between the TSVs. This may be done with oxides or nitrides, similar to wafer preparation for RDLs. After deposition of the passivation layer, a diffusion barrier may be applied to via walls; the material choice is dependent on the conductor material. Again, the barrier also acts as an adhesion promoter for the subsequent layer of conductive material. This is usually copper or tungsten. In some cases it is adequate to cover via walls only, but in most cases a fully filled via is required. The metallization can be done with chemical vapor deposition, physical vapor deposition, electroplating or electroless deposition. Conventional and inkjet based TSV filling method are compared in Figure 7. [10]

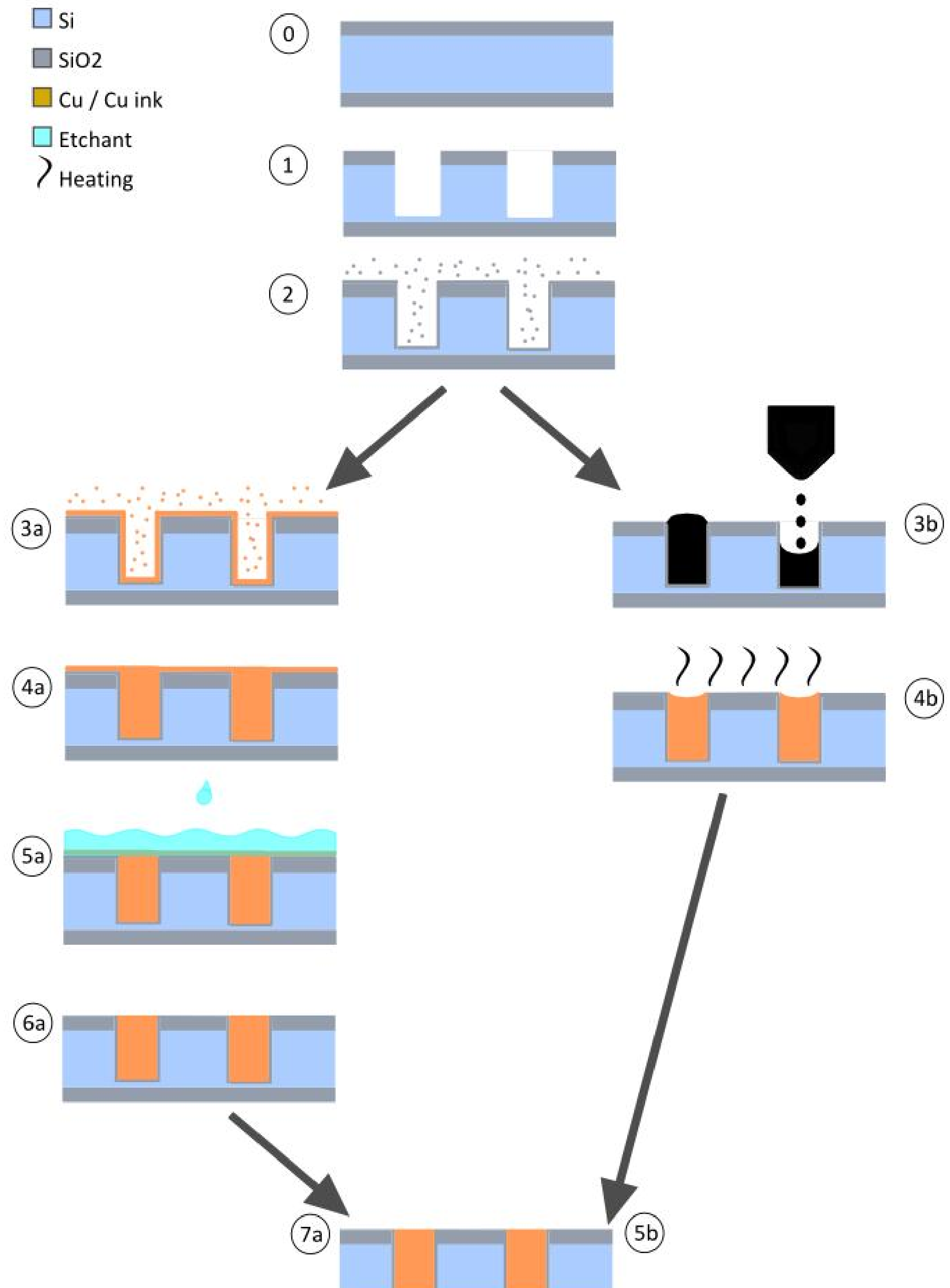

Figure 7: *Conventional TSV filling (a) vs. inkjet filling (b). See body text for explanation of process steps.*

Left hand side of Figure 7 shows via filling with Cu using the conventional manufacturing method (in this case electroplating); on the right hand side, comparable process steps for inkjet filling are shown. In both cases the first three process steps are the same: via drilling using the aforementioned methods and thermal oxidation for via wall passivation. In case of conventional manufacturing method, the process continues with chemical vapor deposition (CVD) or physical vapor deposition (PVD) of Cu seed layer.

This thin layer is deposited to create electrically conductive path for the subsequent step, electroplating. After electroplating, surplus Cu will be etched with suitable etchant and the wafer is thinned to reveal the blind end of the via [10]

The issue with the aforementioned via metallization methods is the slow deposition rate (order of hours). Additional complication is that the removal of excess Cu creates material waste. The inkjet technology might offer some advantages in this regard: fast deposition rate could reduce the filling time and also reduce the material waste. The comparable via filling method using the inkjet is shown on the right hand side of the diagram. The vias are filled with functional nanoparticle ink using a digitally controlled print head. This is followed by sintering phase where the substrate is heated to induce diffusion of nanoparticles and formation of conductive traces to the nanoparticle matrix.

The proposed alternative TSV filling method will result in cost savings due to reduction of material waste and process time. In this case, the process time reduction can be predicted since most of the TSVs are large enough to be filled with conventional piezo based inkjets and there already exists a plethora of print heads with as many as 2000 nozzles. Interested readers are referred to [11] and [12] for more detailed review of TSV filling using inkjet methods.

2.3 Wafer level packaging (WLP)

System level packaging may protect the MEMS devices from contaminants and mechanical stresses during operation, but not during packaging of the devices; an issue which can be remedied with device level protection. For this purpose the MEMS industry has adopted the use of wafer level packaging (WLP). [13]

In WLP the device packaging is done by bonding a capping wafer on top of the wafer containing the devices. This means that the devices are packaged already on the wafer before dicing; WLP process flow is shown in Figure 8 (blue). For comparison, process flow for non-WLP packaging technology is shown as well (green); these type of processes have been used to make for example chip scale packages (CSPs) and quad flat packages (QFPs).

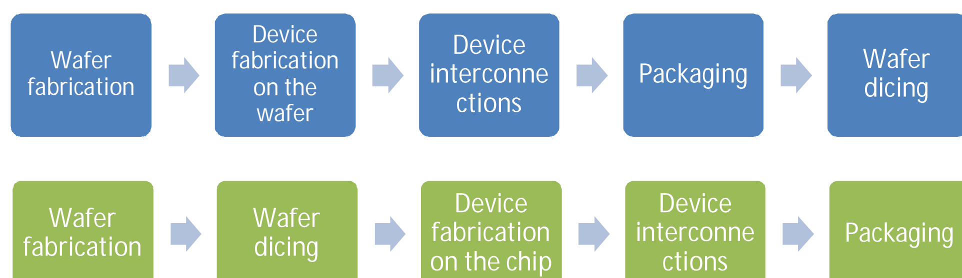

Figure 8: *Process steps for WLP (blue) and non-WLP (green).*

One of the drivers behind the WLP development has been the decreasing size of the electronics devices in general: the WLP is actually a *true* chip scale package with a package footprint exactly the same as the footprint of the chip it contains. For comparison, the CSP is defined as a package with 1.2 times the chip footprint. Additional motivation comes from the potential reduction of fabrication costs: in WLP the interconnection of the devices, the device testing and the device burn-in can be done simultaneously to all devices since they are part of the same wafer. If the microelectronics devices are packaged individually, the tests have to be done separately to each individual chip which means that more testers, handlers and equipment are required for a comparable throughput. These advantages carry over to MEMS packaging as well. However, the WLP offers MEMS packaging some additional benefits beyond miniaturization and cost reduction. Fabrication activities such as dicing *before* packaging may harm the bare device; if the dicing is done *after* the packaging this can be prevented. [5, 13]

3. INKJET PRINTED ELECTRONICS

Printed electronics is a novel area of electronics manufacturing utilizing methods adapted from the graphics industry: inkjet, offset lithography, flexography, gravure and screen printing among others. Common denominator for these is that they utilize inks to additively transfer patterns to substrate using a print file. In printed electronics the inks are functional meaning that they are made of materials such as dispersions of conductive particles and resistive or semi-conductive polymer solutions. When these materials are processed in suitable conditions after the deposition they form electrically functional features. Depending on the pattern and ink, the feature might be a resistor [14], capacitor [15] or transistor [16]; different types of antennas [17] and complex microelectronics package interconnections [18] have been demonstrated as well. [2]

Offset lithography, flexography and gravure printing are so called roll-to-roll printing methods where the substrate is driven through a set of rolls containing the patterns to be printed and the functional ink to make the pattern. This means that the rolls are in contact with the substrate and that the substrate has to bend during processing making it virtually impossible to process materials which are rigid and fragile. Since the RDL will be manufactured on top of silicon wafer, both rigid *and* fragile, roll-to-roll methods are out of the question. This leaves only screen printing and inkjet technology as possible options. Screen printing uses a physical print file as well, but allows for rigid substrates since it contains no rolls: the pattern is transferred through a patterned screen which is placed on top of the substrate. The minimum achievable line width/spacing with this method can be as low as ten microns – just enough for high density RDL. This means that the screen printing could be used for this application as well. [2]

The main advantage of inkjet technology over the aforementioned is that the print file is in digital format instead of physical print plate or roll. This enables contactless deposition of the functional ink and allows for substrates of varying topography, rigidness and fragileness. Although some of these substrates could be used in screen printing, the inkjet has another significant advantage: quick change of pattern design enabling faster change-of-die times and reduced fixed costs of the manufacturing line. This makes the inkjet technology a more attractive solution for additive manufacturing of RDLs. [2, 3]

3.1 Inks

Regarding the high density RDL, the relevant inks are the conductive and dielectric ones. Although both of these can be made from organic or inorganic materials, this chapter will concentrate only on inorganic, metal nanoparticle based conductive inks,

and organic, polymer based dielectric inks. The organic conductive inks are omitted from this study because of their high resistivity and lack of commercial inorganic dielectric inks prohibits their use. [17]

3.1.1 Conductive nanoparticle inks

The conductive nanoparticle inks are comprised of nanosized metal particles dispersed in a solvent and capped with polymer ligands. Some of the common metals are silver, gold and copper; more exotic ones, such as titanium oxide, have been tried as well. Figure 9 shows the basic structure of two nanoparticles dispersed in solvent. The ligands, usually thiols or amines, are used to prevent nanoparticle agglomeration during the storage. The solvents are chosen based on their evaporation temperature, viscosity and surface tension values; a common example would be toluene or tetradecane, but water based inks exist as well. Additives are mixed to the ink to achieve specific functionality: adhesion promoters to increase adhesion between substrate and sintered ink, humectants to prevent unwanted evaporation, biocides to increase the shelf life and wetting agents to increase or decrease the spreading of the liquid on top of the substrate. All these will affect the behavior of the ink at the print head and on the substrate making ink formulation a complex art. [19]

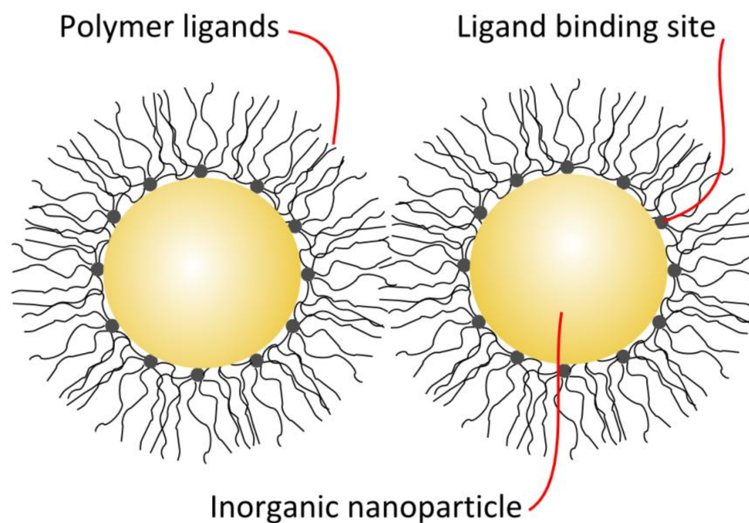

Figure 9: *Nanoparticle with polymer ligands to prevent agglomeration.*

The ability to form conductive traces from high melting temperature metals on top of low melting temperature substrates is based on the minuscule size of the metal particles. The small size induces a so called melting point depression: as the size of the particle is decreased, its melting point will become lower. Although the specific melting mechanism is still unknown, the phenomenon itself has to do with the cohesive energy of the atoms. Since this depends on the number of bonds, the surface atoms with less neighboring atoms, and fewer bonds, have less cohesive energy than the atoms in bulk. As the particle is made smaller, the ratio of the surface atoms to the atoms in bulk increas-

es, the overall cohesive energy decreases and less energy is needed to melt the particle. The effect is striking: silica capped gold nanoparticles were investigated by K. Dick et al and it was found that for five nanometer particles the melting temperature is two hundred degrees below that of the bulk [20]. The problem is that this is still much higher than most substrates can handle. [19]

But the total melting of nanoparticles is not necessary for creating conductive traces. In same way as the melting point decreases as the particles are made smaller, the diffusion rate will increase. Even at lower temperatures there will be diffusion at the interface of two nanoparticles inducing neck growth and coalescence. Since the diffusion rate is high already at relatively low temperatures, protective coating is needed to prevent this from happening before sintering. The polymer ligands are used for this purpose. Hence the break up temperature of the ligands determines the temperature at which the particles start to coalesce and conductive traces start to form. [19]

Ingham et al investigated the process of nanoparticle coalescence for ten nanometer gold nanoparticles capped with oleylamine [21]. They determined three phases for nanoparticle sintering: (1) the melting/desorption or initial aggregation of capping polymer and evaporation of the solvent; (2) diffusion driven neck formation between the particles or final aggregation and (3) continued grain growth. Steps (1) and (2) are shown in Figure 10. Similar process applies for all the *nanoparticle* based inks. In addition to these, there exists also inorganic conductive inks which form conductive traces based on chemical reduction, but these are beyond the scope of this thesis. [19]

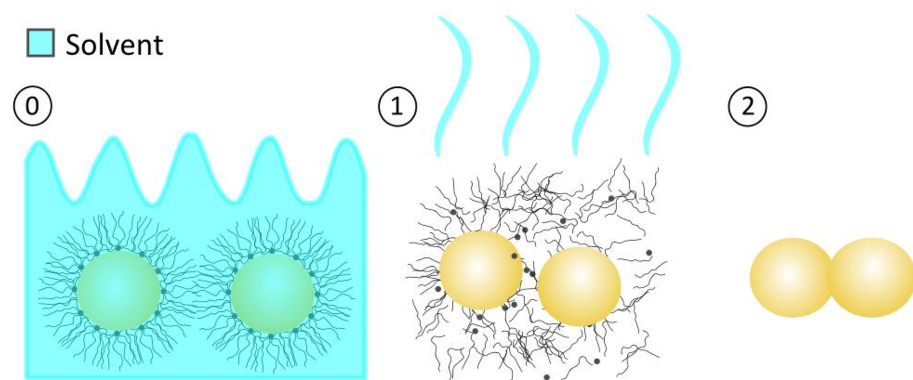

Figure 10: *Nanoparticle coalescence: 1) solvent evaporation and break-up of polymer coating and 2) nanoparticle coalescence.*

The resistivity of the printed trace is usually lower than that of the bulk metal since the time to achieve uniform grain structure is too long from the processing point of view. For example the conductivity of silver nanoparticle ink NPS-J (Harima Inc.) is approximately half of the conductivity of bulk silver when sintered according to the manufacturer instructions [9, 22].

3.1.2 UV-curable dielectric inks

In order to insulate two conductors from each other dielectric inks are needed. Organic, polymer based dielectrics are usually UV-curable, since these have certain advantages over their competitors. [19]

Regarding ink formulation, bulk of it consists of monomers and oligomers which are activated during UV-curing phase to form cross-linked polymer structures. In addition to the monomers and oligomers dispersed in solvent, inks contain photoinitiators which promote the polymerization reaction during UV-exposure and colorants which are important for example in lighting applications since they determine the color of the cured dielectric. Other additives can be introduced to enhance some specific property of ink, such as adhesion, viscosity or wettability. After curing the ink heat is applied to the structure; this is so called hard baking phase which is used to increase the physical, thermal and chemical stability of the polymeric structure. It also evaporates the remaining solvent. Figure 11 shows the process steps of preparing the UV-curable inks after ink has been deposited on the substrate. [19]

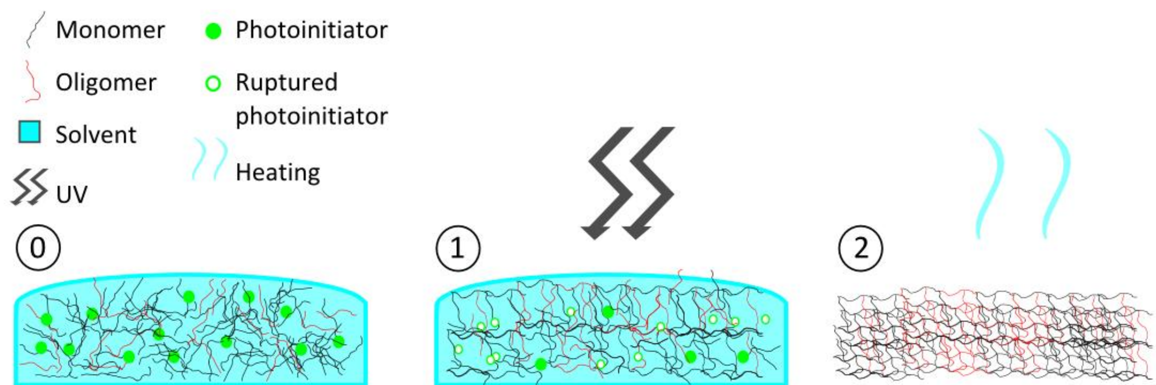

Figure 11: *Main process steps for UV-curable dielectric ink: 1) UV-curing and 2) hard baking.*

Based on the previous, both dielectric and conductive inks are very complex entities. To formulate inks specifically for a chosen purpose and to control all relevant parameters would require specialized know-how and is thus beyond the scope of the thesis. Instead, commercial products were used.

3.2 Conventional inkjet technologies

It is important to understand the operating principles of the conventional inkjet technologies in order to understand their limitations and appreciate why an electrohydrodynamic inkjet printer, such as the SIJ, had to be used for fabrication of a high density RDL.

3.2.1 Continuous inkjet (CIJ)

As mentioned in the introduction, the continuous inkjet (CIJ) was the earliest example of inkjet technology. A schematic of CIJ is shown in Figure 12. In CIJ, a continuous jet of ink is ejected from the print head by applying pressure to the ink reservoir. The ink will separate to droplets since the jet will try to achieve lowest possible energy state by minimizing its surface energy - effect known as Plateau-Rayleigh instability. This natural effect can be further controlled by inducing disturbances on the jet enabling volume control of the ejected droplets. Before the break up occurs, forming droplet is charged at charging electrode where the applied voltage will determine the amount of induced charge. When the droplet ultimately breaks up, it will carry the charge with it. Next in line are the deflection plates with a fixed voltage. Uncharged droplets will not be affected by them, but will carry on to the droplet collector, or gutter, for re-use. The charged droplets, however, will be deflected according to the amount of charge they contain. The amount of deflection will create the dimensions of the pattern. [3]

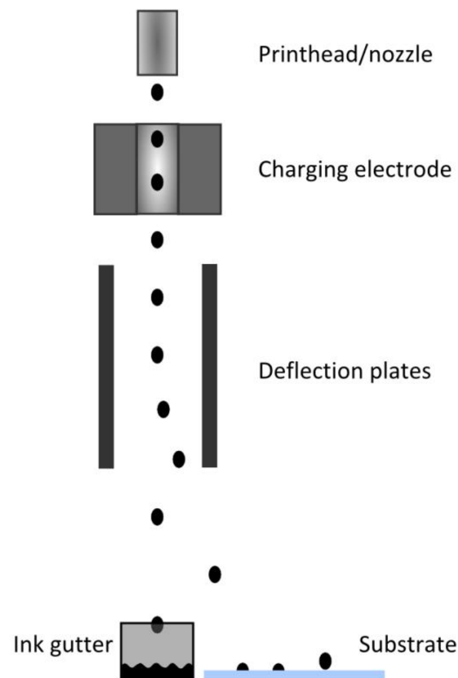

Figure 12: *CIJ operating principle.*

It is clear from above, that the mechanism behind the CIJ droplet positioning is quite complex and in this case the complexity translates to a relatively low resolution. The drop-on-demand inkjets manage to improve this by taking a more simplistic approach to droplet generation and deposition. [3]

3.2.2 Drop-on-demand (DoD) inkjets

DoD printers make do without the complicated charging/deflection mechanisms by producing droplets only at chosen moments. The resolution is improved since the point of deposition is determined by the print head movement relative to the substrate and not by the droplet flight path. [3]

In these devices the droplet ejection happens either through piezoelectric or thermal actuator inside the ink chamber. The chamber is connected to ink reservoir by a large channel called the throttle and to environment with a smaller channel called the nozzle. A pressure pulse will be generated inside the chamber by voltage controlled expansion of a piezoelectric element (see Figure 13) or a thermal bubble generated by a voltage controlled resistor. The pressure pulse will drive the ink out of the nozzle since the volume, and the mass, of the liquid inside the nozzle is significantly smaller than the mass of the liquid inside the large throttle. The speed of the ejected droplet can be controlled by varying the height of the voltage pulse; this is an additional improvement over the constant droplet speed CIJ. [3]

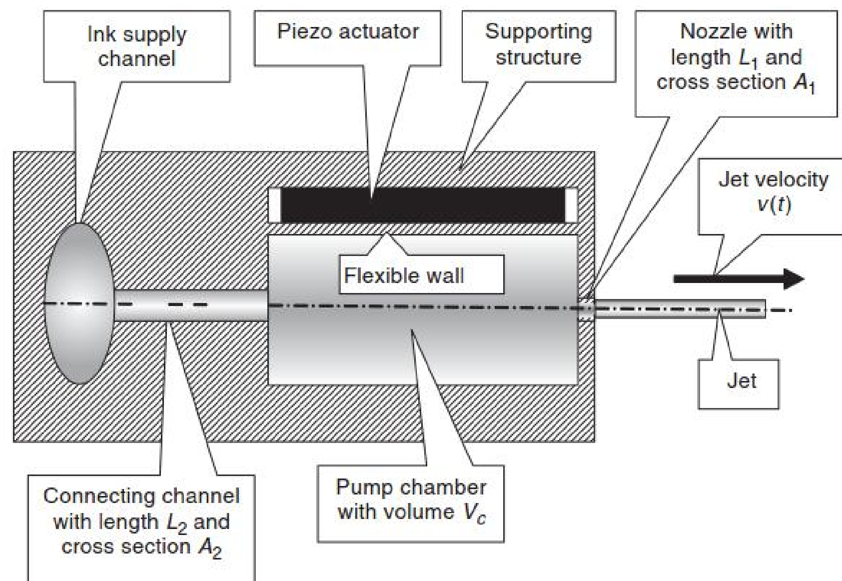

Figure 13: *The operating principle of piezo head [3].*

Although the resolution can be improved by using the DoD instead of CIJ, it will still be too low for the high density RDL. The ultimate resolution limit in both cases is set by interplay of ink specifications and physics of droplet generation; window for suitable ink parameters will become smaller as the magnitude of pressure pulse is increased to achieve higher resolution. Large pressure is necessary since small droplets can be only generated using small diameter nozzles. To eject liquid through a small opening neces-

sitates larger forces than the ejection through wider opening. In other words, the magnitude of the pressure pulse has to increase and the ink formulation will become virtually impossible. [3]

Because of this, droplet volume of conventional inkjets is limited to approximately one picoliter. However, it is possible to circumvent this limit to some extent with various substrate surface modification methods, such as predefining surface energies [23] and increasing the substrate temperature [24]. But the result will still be over 20 microns – double the allowed maximum conductor width of high density RDL. To overcome this limit, the mechanism behind the droplet ejection has to be changed.

3.3 Super Inkjet (SIJ)

SIJ draws its heritage not from the graphics industry, but from the electrospraying technology used for atomization of liquids. It is a novel type of electrohydrodynamic (EHD) printer, which utilizes oscillating electric field to generate the necessary pressure for droplet ejection. This mechanism enables the generation of sub-femtoliter droplets, which translates to a resolution of approximately one micron on the substrate if the wetting conditions are suitable. But before describing the operating principle in more detail, a short description of the machinery is in order. [4]

3.3.1 Machinery

Simplified, the equipment consists of a glass nozzle containing the ink, a charging conductor running through the nozzle, a moving xy-plate and the electronics for controlling the charging conductor voltage, the nozzle-to-substrate distance and the xy-plate plate movement. A visual interpretation of the SIJ functional parts is shown in Figure 14. The following list states the function of the parts. [4]

Figure 14: *SIJ parts and their functions. E denotes the electric field between nozzle and grounded xy-plate.*

1. Nozzle. The nozzle is a fine capillary tube made out of glass due to its ease of molding. It comes in three different sizes: Super Fine, Standard and Large Nozzle. Each size has a specific nozzle tip diameter, target droplet size and line width: 1-3 μm, 5-10 μm and 15-20 μm, respectively.
2. Charging electrode. In conventional EHD printers, the nozzle was usually made of metal and could also act as an electrode, but because glass is dielectric the ink has to be charged via a conductor placed inside the nozzle.
3. Functional ink (see Chapter 3.1), charged with the charging electrode.
4. Magnetic nozzle holder. The nozzle has a metal collar which attaches to the holder.
5. Computer to choose the printing parameters.
6. Waveform generator to generate a certain voltage waveform. The waveforms that can be generated are square waves with three different duty cycles, sine wave and triangular wave.
7. High voltage amplifier for generating the necessary voltage. The operational range is from -2.57 kV to +2.57 kV.
8. Substrate. This can be either conductive or non-conductive as long as the permittivity is suitable.
9. Moving xy-stage. Three different types exist: vacuum, heated and normal stage. These are electrically connected so that the potential difference between the stage and the ink in the nozzle can be biased on a certain level. [4]

3.3.2 Operating principle

Simplified, the operating principle is as follows: ink inside the nozzle is charged by applying current to the charging electrode; amount of charge determines the strength of the electric field between the ink meniscus at the tip of the nozzle and the substrate; if the field is strong enough, it will pull out a droplet. The charging of the ink is done by applying a pulsed voltage to the charging electrode. Thus, each pulse should generate a droplet. [4]

A more detailed understanding of the operating principle requires a quick review of EHD devices since the SIJ is derived from these. *The conventional EHDs operate in a Taylor cone mode*. Taylor cone is an ink protrusion formed at the tip of the nozzle when the ink is charged relative to the substrate (see Figure 15). If the electric field is large enough, a continuous jet of ink starts to eject from the apex of the cone. This occurs when the following equation is satisfied:

$$d > \frac{\pi\gamma}{\epsilon_0 {E_0}^2} = \frac{\pi\gamma h^2}{\epsilon_0 V^2} \left(or \Rightarrow V > h\sqrt{\frac{\gamma\pi}{\epsilon_0 d}}\right) \quad (1)$$

where d is the diameter of the nozzle, γ the surface tension of the liquid, ϵ_0 the dielectric constant of vacuum and E_0 the electric field between the nozzle and the substrate. The latter is equal to the nozzle-to-substrate voltage (V) divided by the nozzle-to-substrate distance (h). If the diameter of the nozzle is made small enough, the Taylor cone will not form and the jetting becomes impossible. This is due to practical limitations imposed on the nozzle-to-substrate distance and magnitude of the voltage. For a while it was thought that this limitation can't be overcome. [4]

The SIJ uses a very small diameter nozzle to overcome the limitation. When the diameter of the nozzle is small enough, the hemispherical ink protrusion at the nozzle tip becomes so small that the equation (1) is no more applicable. The reason for this is that instead of the macroscopic electric field E_0, a local electric field E_{loc} is effective. This depends on the nozzle form factor ($1.5 < k < 8.5$), the ink meniscus curvature ($p \cong d/2$) and the nozzle-to-substrate voltage (V) according to:

$$E_{loc} = \frac{V}{kp} = \frac{2V}{kd}. \qquad (2)$$

If the equation (2) is compared to that of the macroscopic field ($E = V/h$), the local electric field becomes significantly larger compared to the macroscopic field when the nozzle diameter is reduced to $d \ll h$. In this case the electrostatic pressure caused by the local electric field is large enough to pull droplets out of the nozzle *without using the Taylor cone mode, but electrostatic suction.* Comparison of conventional EHD and SIJ is shown in Figure 15. [4]

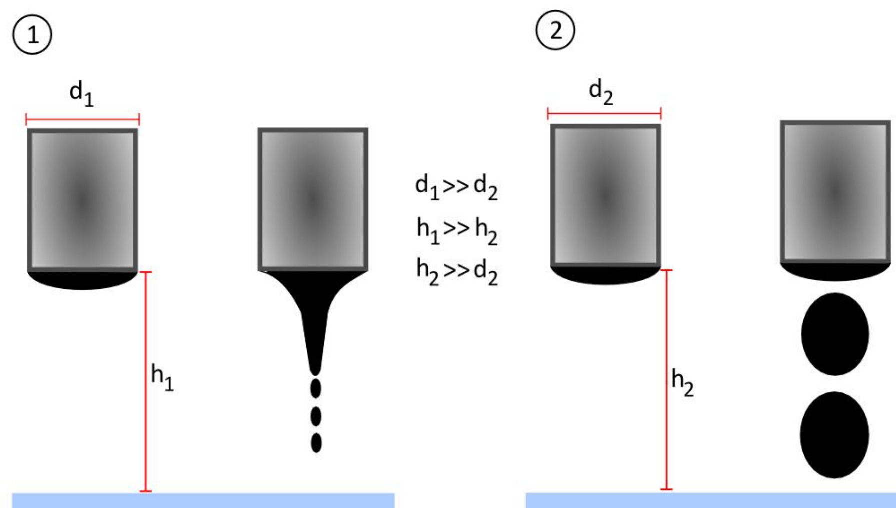

Figure 15: *Conventional EHD (1) vs SIJ (2) shown with and without ink charging. In conventional EHD a Taylor cone forms; in SIJ electrostatic suction ejects droplets. Note that (1) and (2) are not drawn in same scale.*

In SIJ, the condition for droplet ejection is satisfied, when the electrostatic pressure (P_e) is larger than the pressure caused by surface tension (P_s). This leads to the following condition for minimum ejection voltage:

$$V > \sqrt{\frac{\gamma d}{2\epsilon_0}}. \tag{3}$$

From equation (3) it can be seen that reducing the diameter of the nozzle also reduces the voltage necessary for droplet ejection. The nozzle diameter – minimum ejection voltage relation for the SIJ is shown on the left hand graph of Figure 16. For comparison, the right hand side shows this relation for the conventional EHD printer. [4]

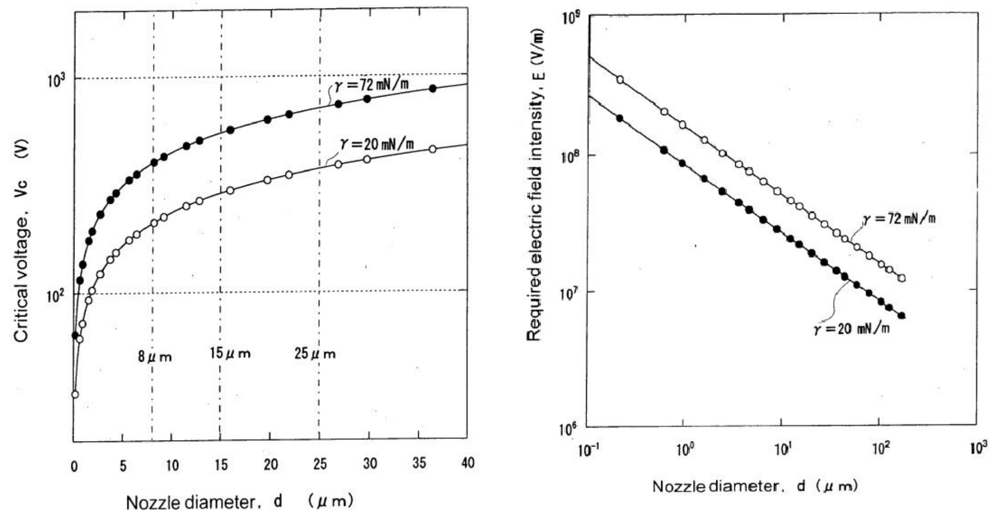

Figure 16: *Comparison of jetting behavior of SIJ (left) and conventional EHD printer (right). The critical voltage marks the minimum voltage and the "required electric field intensity" the minimum electric field for ejection. [4]*

When the macroscopic electric field becomes large enough, the operation mode of SIJ will be that of the conventional EHD printer i.e. a Taylor cone will form. This is to be avoided, since the Taylor cone has various instabilities and is thus difficult to control [23]. Combining equations (1) and (3) gives the following relation for the suitable nozzle-to-substrate voltage values:

$$h\sqrt{\frac{\gamma\pi}{\epsilon_0 d}} > V > \sqrt{\frac{\gamma k d}{2\epsilon_0}}. \tag{4}$$

The ejection voltage is determined by the amount of charge accumulated to the nozzle tip and the frequency of the ejection by the frequency of the oscillating voltage. This means that the charging rate of the ink becomes a limiting factor. In other words, *there is a cutoff frequency (f_{high})* which depends on the dielectric relaxation time (τ). This, on the other hand, depends on the permittivity of the ink (ε), and the ink conductivity (σ):

$$f_{high} = \frac{1}{\tau} = \frac{\sigma}{\varepsilon}. \tag{5}$$

It has to be noted here, that at higher frequencies the droplet generation might not occur during each pulse. Even if the ink were a perfect conductor with $\tau = 0$, the finite viscosity, surface tension and specific gravity will cause the droplet generation frequency to deviate from the voltage frequency. This means that at high frequencies the SIJ is not necessarily a *drop-on-demand* printer. The droplet volume can also be expected to vary with the charging frequency. The duty cycle of the pulse will decrease with increasing voltage. This means that at high frequencies the meniscus has less time to gather the necessary amount of charge for droplet ejection. Since all real inks have a finite charging rate, less charge will be gathered at the meniscus and the electrostatic force which generates the droplet will decrease. This leads to inverse relationship between droplet volume and the charging frequency. [4, 26]

The lower limit for the frequency (f_{low}) is determined by the speed of the substrate (v_s) and the radius of the droplet on the substrate surface (r_d). At the limit, the ejection frequency is so small that the successive droplets will not overlap to create a continuous printed line. A simplistic way to put this is:

$$f_{low} = \frac{v_s}{2 * r_d}. \tag{6}$$

If it is assumed that each pulse will generate a droplet, then the suitable frequency range is determined by combining equations (5) and (6):

$$\frac{v_s}{2 * r_d} < f < \frac{\sigma}{\varepsilon}. \tag{7}$$

The challenge in using equation (7) is the determination of r_d, since it depends heavily on the drop volume and the surface properties. Because the effects of surface properties (mainly surface energy and the surface roughness) are well understood at the moment, the main challenge is to determine how different parameters affect the volume of the droplet and the resulting conductor width. Since there exists no physical formula with enough predictive power, statistical analysis based on design of experiments approach has to be applied. [4]

3.3.3 Suitable parameter values

In previous chapter guidelines for the parameter values were determined. Table 2 recapitulates these for the voltage and frequency. The suitable values for nozzle-to-substrate distance are based on experience. If the nozzle-to-substrate distance is increased signifi-

cantly over 100 µm unstable jetting will occur. If the distance is reduced too much, external vibrations will cause the nozzle to hit the substrate thereby breaking it. Table 3 shows the explanations for the parameter abbreviations. [4]

Table 2: *Suitable values for peak voltage, frequency, and nozzle-to-substrate distance.*

Parameter	Suitable values	If larger	If smaller
Nozzle-to-substrate voltage	$h\sqrt{\frac{\gamma\pi}{\epsilon_0 d}} > V > \sqrt{\frac{\gamma k d}{2\epsilon_0}}$	The jetting happens in Taylor cone mode which is instable.	The jetting stops
Frequency	$\frac{\sigma}{\varepsilon} > f > \frac{v_s}{2 * r_d}$	Jetting stops	Separate droplets on the substrate surface
Nozzle-to-substrate distance	$h < 100\ \mu m$, but preferably $h \leq 30\ \mu m$	Accuracy of landing deteriorates	Nozzle hits the substrate when vibrations occur

Table 3: *Explanation for terms in Table 2.*

Term	Explanation	Term	Explanation
h	printing height	v_s	speed of the substrate
γ	surface tension of the ink	r_d	radius of the droplet on substrate surface
ϵ_0	dielectric constant	f	frequency
V	nozzle-to-substrate voltage	σ	conductivity of ink
k	the nozzle form factor (between 1.5 and 8.5)	ε	dielectric constant of ink

3.3.4 Operating the equipment

Operating the equipment is in principle very straight forward as can be seen in Figure 17. The process steps are described here only in a general sense, since a detailed explanation can be found from the manual.

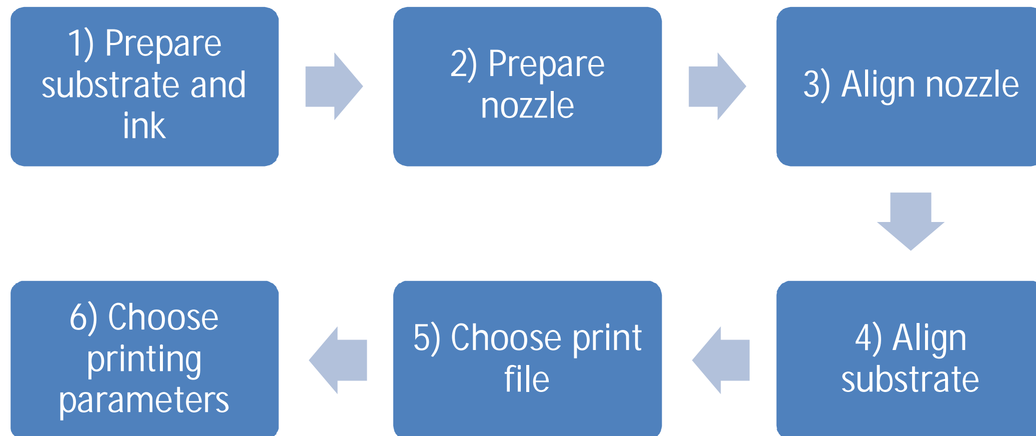

Figure 17: *Process steps for printing preparation.*

1. The substrate is cleaned and treated to achieve the required wetting behaviour. If the surface hydrophobicity is increased, the wetting angle of the drop decreases and it spreads less; if it's decreased, there will be more spreading. Hydrophobicity can be decreased with UV-Ozone or siloxane treatment. The cleaning is usually done by wiping the surface with isopropanol. Deionization might also be necessary, especially in case of dielectric substrates, such as plastics and oxide coated silicon wafers, since charge tends to accumulate on the substrate surface. Otherwise this will affect the jetting behaviour.
2. The nozzle preparation means the filling of the nozzle with suitable ink. Because the size of the nozzle is very small, a microloader filling kit has to be used; these are provided for example by Eppendorf GmbH. It must be made sure that the ink flows all the way to the tip of the nozzle; otherwise, the electric field will not be able to pull it out. Air bubble formation must also be avoided.
3. The nozzle alignment consists of two steps. First, correct nozzle-to-substrate distance is determined. This is done with a help of the side view camera. Nozzle printing height can be determined by reducing the nozzle-to-substrate distance so that the nozzle almost touches the surface and increasing the z-position by 100 microns (or less). Second step is to align the alignment camera and the nozzle. This is done in order to find right printing starting point using the alignment camera.

4. Because the substrate may be tilted in horizontal direction in comparison to the xy-stage, the tilt has to be corrected. This is done with the alignment camera by determining two spots on the substrate which should have the same y-coordinate. Then the actual y-coordinates are measured and the angle is calculated using these values.
5. The print file is a simple txt-file. It contains all the necessary information regarding the structure geometry. It also determines which nozzle holder (four possibilities) and what parameter sets (nine all in all) are to be used. The txt-file can be generated straight from a dxf-file, although this has certain limitations.
6. The actual printing parameter values are not specified in the print file, but in software user-interface. Following printing parameters can be adjusted: waveform, amplitude voltage ($Vmax$), bias voltage ($Vbias$), frequency (f), printing speed (v) and nozzle-to-substrate distance (h). For nozzle purging purposes, it is also possible to define a spit voltage and time. Figure 18 shows a graphical interpretation of $Vmax$, $Vbias$ and f.

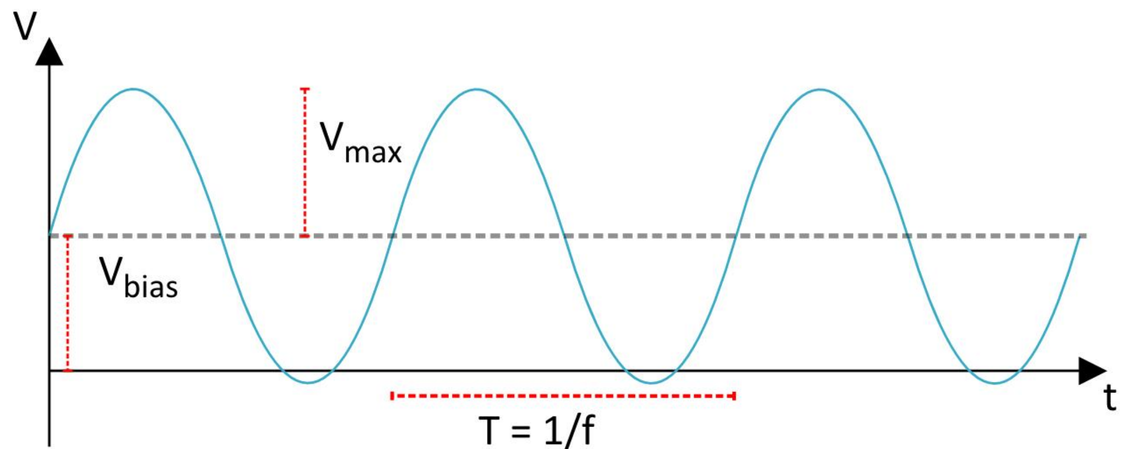

Figure 18: *Description of applied voltage for sine waveform.*

3.4 Conventional DoD printers vs. SIJ

In conventional technologies the spreading of the droplet (printing resolution) depends on the following parameters: the viscosity and surface tension of the ink, the kinetic energy of the droplet, the surface energy of the substrate and the volume of the droplet. In most cases, the resolution is improved by surface energy modifications or by reducing the droplet volume by using a smaller nozzle. However, it is not possible to control the resolution during the inkjet operation. [3]

In SIJ this is possible, since the droplet volume depends on the strength of the electric field. There are, however, some unwanted side effects to this type of working principle: since the ink may retain a charge after the deposition, this charged feature can affect the droplet volume during the printing of the second layer. In a sense, there is coupling between what has been printed on the substrate and what will be printed. Otherwise the

parameters affecting the droplet spreading in conventional DoD and SIJ are very much the same. [4]

Some of the important differences between the conventional DoDs and the SIJ are shown in Table 4.

Table 4: *Conventional drop-on-demand inkjet printers versus the Super Inkjet.*

Parameter	**Conventional DoD**	**SIJ**
Droplet volume	>1 pL	0.001-10 pL
Resolution	> 50 µm	> 1 µm
Ink viscosity	1-20 mPa*s [3]	1-10000 mPa*s [25]
Droplet generation principle	Pressure wave inside the ink chamber	Electric field outside the ink chamber
Characteristics of printing	Droplet size determined mainly by nozzle diameter à effect of printing parameters is not that significant	Droplet size determined by the parameters which affect the electric field à droplet size can be varied significantly during printing
	Environmental conditions do not affect the droplet size heavily	Environmental conditions (f. ex. humidity) affect the droplet size by changing the strength of the electric field
	Droplet size is not affected by the substrate composition	Droplet size is affected by the substrate composition, specifically by substrate permittivity
	Pre-deposited droplets do not affect the droplet size	In case of insulating substrate, the pre-deposited droplet retains charge and will affect the droplet size
	No electrowetting	Electrowetting will decrease the contact angle in case of insulating substrate

4. SIJ PROCESS OPTIMIZATION

The SIJ process optimization starts with choosing the suitable conductive inks. Although datasheet values (viscosity etc.) of the ink would suggest that it is suitable for SIJ, this isn't necessarily so; for example, ink instabilities affect the print result. Simple stability tests were done for preselected inks to find out the most suitable candidate for SIJ printing. This is discussed in chapter 4.1.

From the electrical characteristics (resistance, RF-behavior etc.) point of view it is important to be able to control the width, thickness and edge roughness of the conductors. It should be possible to predict these if only the droplet size and wetting properties of the substrate would be known. The wetting behavior can be easily measured, but the droplet size of the SIJ is affected by such a variety of parameters that it is impossible make accurate predictions based on theory alone. Therefore, statistical analysis has to be carried out in order to find out the effect of different parameters on the conductor width, thickness and resistance: topic of chapters 4.2 and 4.3.

This is followed by a showcase of two printed single layer RDL demonstrators in chapter 5.

4.1 Suitable inks

The RDL is usually made of aluminum, copper or gold. In some cases silver might be used. Commercial copper nanoparticle inks were found to be unsuitable for SIJ processing. Some commercial aluminum nanoparticle inks exist, but because of their rarity the focus here was on gold and silver inks. The selected inks represent both low and high sintering temperature variants and the three most common solvents. Table 5 shows the material and processing parameters for these. NPS-J and NPS-JL are products of Harima Chemicals, Inc.; CAg-2000 and CAu-2000 products of ULVAC Technologies, Inc distributed by SIJ Technology Inc.; DGP 40LT-15C a product of Advanced Nano Products Co.

Table 5: *Inks for stability testing.*

Ink	Nanoparticle material	Solvent	Resistivity (µOhm*cm)	Viscosity (mPa*s)	Solid content (wt%)	Sintering parameters
CAu-2000 (ULVAC) [28]	Au	Cyclododecene	8	10	50	1h @ 250ºC
CAg-2000 (ULVAC) [28]	Ag	Tetradecane	3	10	58	1h @ 230ºC
NPS-J (Harima) [22]	Ag	Tetradecane	3	9	65	1h @ 220ºC
DGP 40LT-15C (ANP) [29]	Ag	TGME*	11-12	10-17	30-35	0,5-1h @ 120-150ºC
NPS-JL (Harima) [22]	Ag	TGME*	6	11	30-35	1h @ 120 ºC

* Triethylene glycol monomethyl ether

4.1.1 Test for ink stability

The suitability of the ink was determined by two aspects: *the jetting has to be stable in a sense that it must not stop during printing* and *it must create uniform lines*. The uniformity requirement means that no splashes, discontinuities or extensive edge roughness may be present in the conductors.

Different inks were tested in a quick and dirty trial where 150 separate lines were printed on top of oxygen-plasma cleaned Ti/W coated silicon wafers. The trial was repeated ten times for each ink. The measure of stability is the number of conductors which can be printed before the jetting stops.

In order to get comparable results, the line width was calibrated to ten microns for all the inks by varying V_{bias} and V_{max} while keeping the other parameters constant; this meant voltage waveform and frequency, printing speed, nozzle-to-substrate distance and the nozzle type. The humidity was controlled as well.

4.1.2 Stability test results

The results of the test are shown in Figure 19 as an average degree of completion of the ten trial structures.

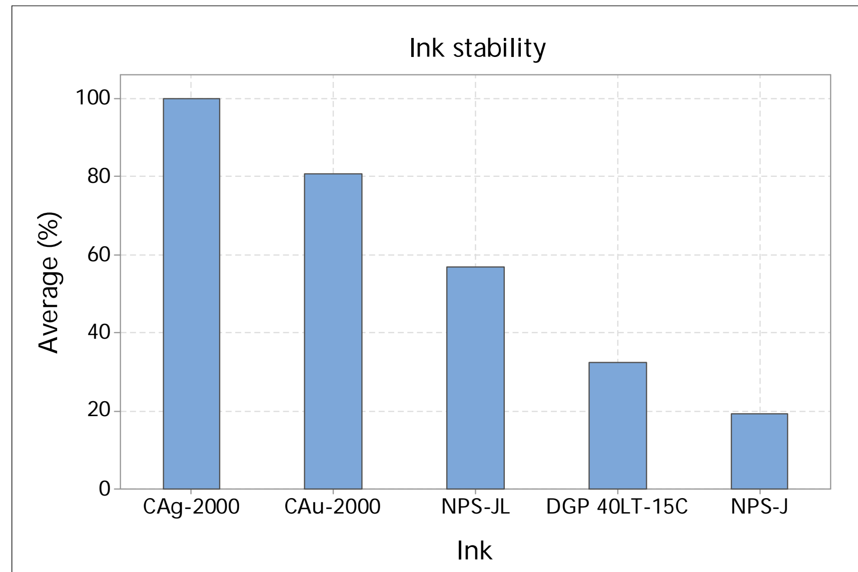

Figure 19: *The stability of silver inks shown as an average degree of completion of the ten test structures.*

It seems that the CAg-2000 (ULVAC) is by far the most stable of the four silver inks when it comes to jetting stability: the jetting didn't stop in any of the test structures. However, as shown in Figure 20, the width varies drastically between subsequent conductors. Additionally, the uniformity of the conductors is very poor and the jetting does not start where it should. This type of behavior is unacceptable. It must be noted here though, that the tested ink was quite old and this may have caused the observed erratic behavior.

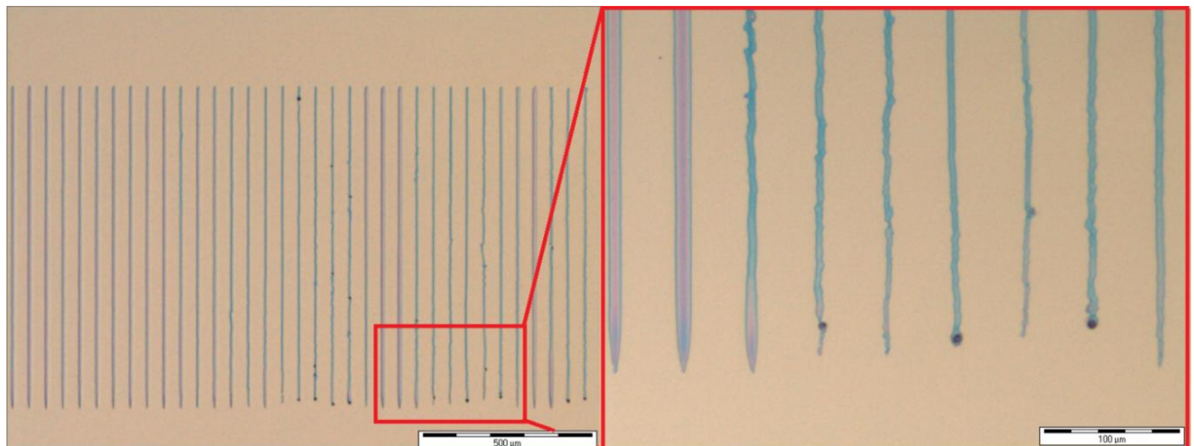

Figure 20: *Stability of CAg-2000. The jetting doesn't stop, but the uniformity of the conductors is poor. Also the starting point of jetting is not where intended and the conductor width varies constantly.*

With NPS-JL on average 56% of the structure can be printed before the jetting stops. As shown in Figure 21 the uniformity of the conductors is improved over that of CAg-2000. In three test structures jetting didn't stop at all and the conductor width increased towards the end significantly. This is unacceptable. However, the other structures showed decreasing conductor width towards the end. Paleness of the conductors is due to the extremely thin material layer and the fact that the sample had time to dry up completely before the picture was taken.

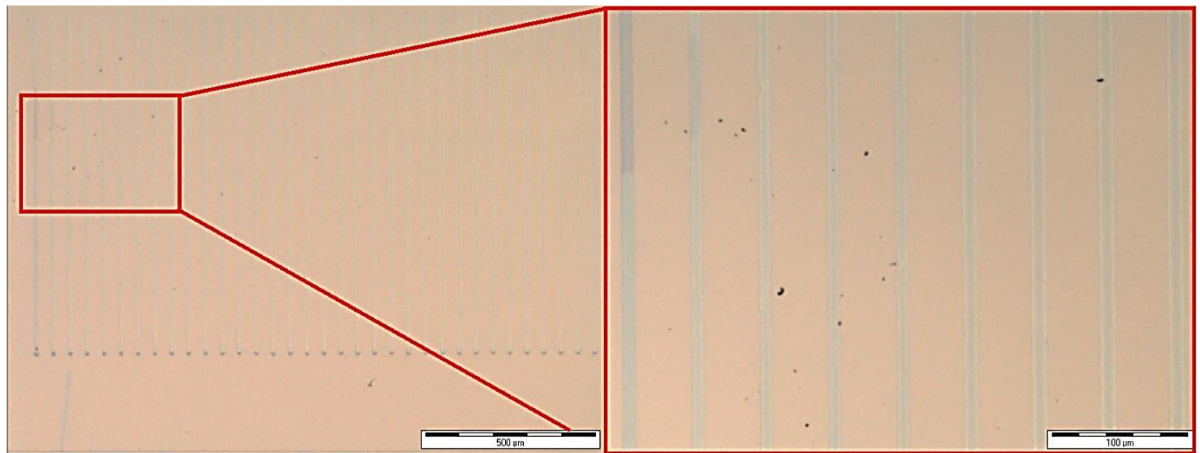

Figure 21: *Stability of NPS-JL. The uniformity of the conductors is good. In some cases the width increases significantly as the printing proceeds.*

With DGP 40LT-15C on average 32% completion rate was be achieved. As seen in Figure 22, the conductor width varies significantly during printing. The uniformity of the lines is very poor as well. Again, this is unacceptable.

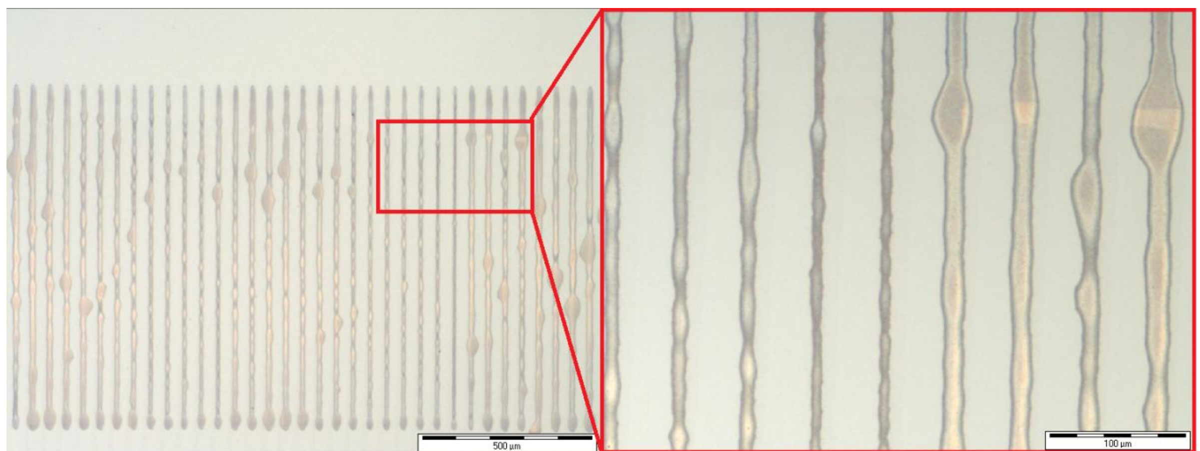

Figure 22: *Stability of DGP 40LT-15C. The jetting doesn't stop, but the uniformity of the conductors is poor and there is significant width variation.*

The NPS-J produces the worst jetting stability of the test set (see Figure 23): on average only 20 percent of the conductors will be printed. However, the uniformity of the conductors is very good and the calibration accuracy is very good as well. There is insignificant width variation during the printing. It is interesting to note, that there

seems to be significant variation between CAg-2000 and NPS-J although they both use tetradecane as a solvent, have similar solid content and similar viscosity. The reason for this difference is not clear.

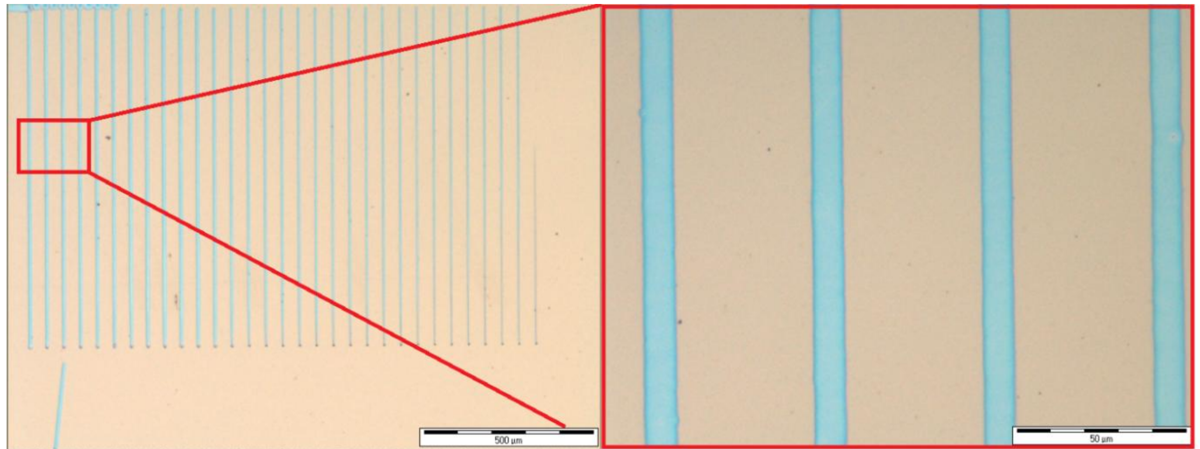

***Figure 23:** Stability of NPS-J. The jetting stops during the printing but the conductors are very uniform.*

With the gold ink CAu-2000 (ULVAC) on average 80% of the conductors can be printed before the jetting stops. This is a very good value. Additionally the conductors seem to be very uniform and the width varies very little (see Figure 24). The calibration accuracy is good as well.

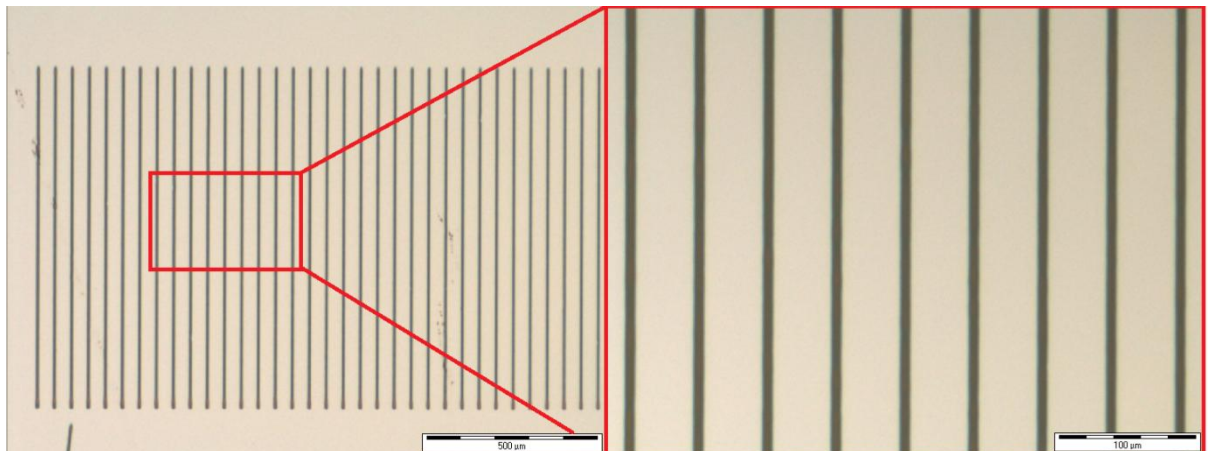

***Figure 24:** Stability of the gold ink CAu-2000. The stability of jetting is very good as is the uniformity of the conductors.*

4.1.3 Conclusion

On top of Ti/W-coated silicon, all the Ag inks seem to produce mediocre results. Either the stability of jetting or the uniformity of conductors is poor. In the actual RDL it is important that both of these are well under control. The poor uniformity increases the capacitive losses in high frequency applications and the poor stability makes the print-

ing of hundred or so conductors of a single RDL an arduous task. The only aspect speaking on behalf of the silver inks is their somewhat lower resistivity compared to gold inks.

The Au ink CAu-2000 seems to produce the best results if both the uniformity and stability of conductors is considered. Since the existing processes in MEMS manufacturing are optimized for Au instead of Ag, it makes sense to do the further testing with this ink.

4.2 Conductor width

The effects of different parameters on conductor width were estimated using the design of experiments (DoE) approach and Minitab statistical analysis software. For this purpose, conductors were printed with a specified set of parameters and their widths were measured from four random points with an optical microscope using a 50X objective. The resulting width is an average of these four measurements. The measurement accuracy is approximately one micron.

The idea of DoE is to find out the correlations between inputs and outputs of a system. This is done by varying the input levels and measuring the output produced by the system. Number of runs compared to the number of input variables determines the accuracy of the produced model. It also determines how reliably the model estimates effects of multiple factor interactions – this is also called the resolution of the design. The best accuracy and resolution is achieved by using a so called full factorial design where all possible input combinations are investigated. It is also important to replicate the procedure. [30]

In practice however, this will be very time consuming. Usually the important factors are first identified with a lower resolution factorial design consisting of fewer runs and a higher resolution design is performed only for these parameters to find out a more accurate model. Since the two level factorial designs can only estimate linear effects, it is common to use multi-level response surface method as the higher resolution design to detect possible curvature of the model (quadratic effects etc.). This is also the current approach. [30]

4.2.1 Significant parameters

In the current case output is the width of the conductor; system is the SIJ electrohydrodynamic printer and inputs are the parameters which are thought to affect width. Seven principal parameters were identified for analysis. These are given in Table 6 with the justification for selection.

Table 6: *Principal parameters affecting the conductor width.*

Parameter	Justification for selection
V_{max}	Increasing voltage increases the strength of the electric field. This increases droplet volume and conductor width.
V_{bias}	See above.
Frequency	Increasing frequency of droplet ejection should increase the number of droplets per unit length, thus increasing the conductor width.
Waveform	Increasing duty cycle of voltage pulse should enable generation of larger droplets resulting in wider conductors.
Printing speed	Increasing the printing speed should reduce the number of droplets per unit length thus decreasing the conductor width.
Nozzle-to-substrate distance	Increasing the distance should weaken the electric field and decrease the conductor width.
Humidity	Increasing the humidity should decrease the strength of the electric field by increasing the relative permittivity of the air. The conductor width should therefore decrease [34].

After selecting the principal parameters, suitable DoE design was chosen. Since varying the humidity is time consuming, a split plot factorial design was used. In this type of design the hard-to-change parameter is kept constant in each block while other parameters are varied. Using two levels for each parameter, going through half of all the possible parameter combinations and replicating this procedure once resulted in a design with VII resolution. This means that all linear interactions up to 4-factor interactions can be reliably distinguished from each other, but they may be aliased with 5-factor (and higher) interactions. A description of all the runs with corresponding output measurements is given in Appendix A.

The results show that all the parameters have a significant effect on the conductor width. This can be seen in Figure 25 which is s a half normal plot for standardized effects for the parameters; further the parameters are from the fitted line, the stronger they affect the conductor width. Varying the waveform and distance seem to have the most significant effect, whereas printing speed, V_{bias}, V_{max} and frequency affect the width comparably little. It is also interesting to note that the humidity in itself doesn't affect the width, but combined with V_{bias} it does; in other words, one-way interaction is missing. However, this is only a minor inconvenience since the analysis clearly shows that the humidity does affect the width - be it then through one-way *or* two-way interaction. Thus, it shouldn't be excluded from further analysis.

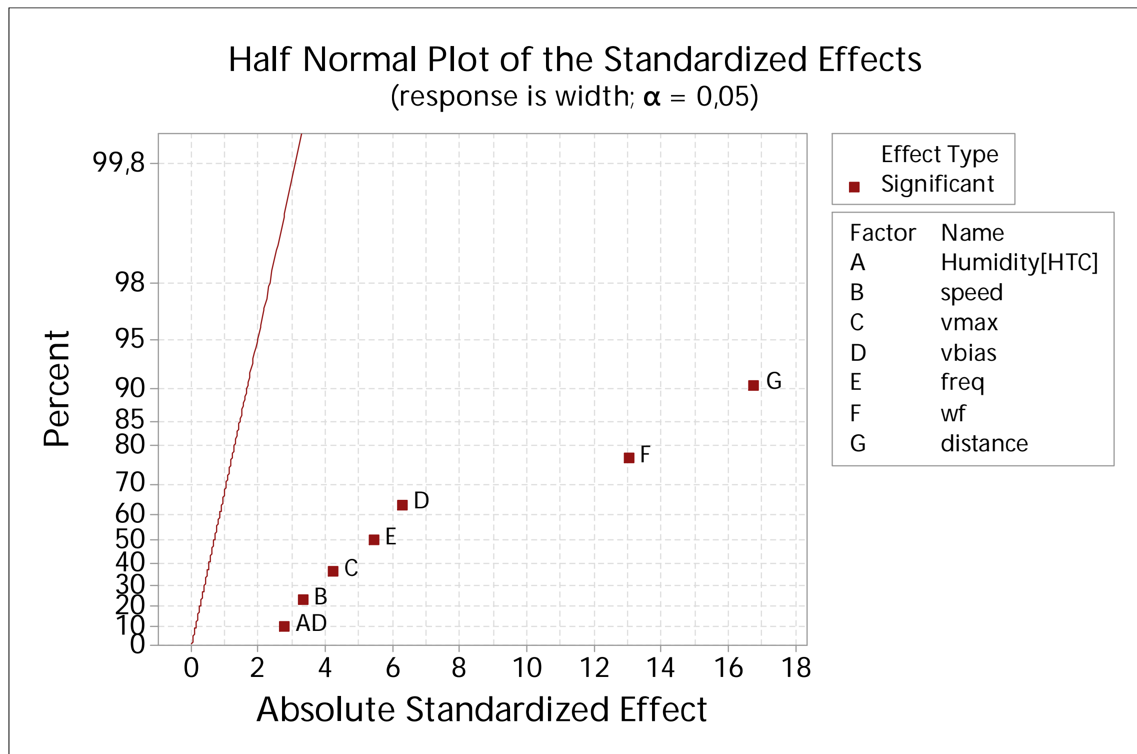

Figure 25: *Standardized effects for the chosen parameters.*

The main effects, their direction and strengths are shown in Figure 26. Here it seems that the humidity in itself does indeed have an effect on width. Contrary to Figure 25 the effect is the strongest one recorded. Also the direction of the effect is contrary to what was predicted in Table 6. The frequency seems to have an inverse effect as well. This could be explained by the decreasing length of each pulse as the frequency is increased since similar effect can be seen when the waveform is changed from sine to triangle. As the length of the pulse decreases, the ink meniscus has less time to charge up and the effective electric field will be weaker compared to longer pulse. This will decrease the droplet size and conductor width. Effects of printing speed, V_{bias} and V_{max} are similar to what was predicted in Table 6.

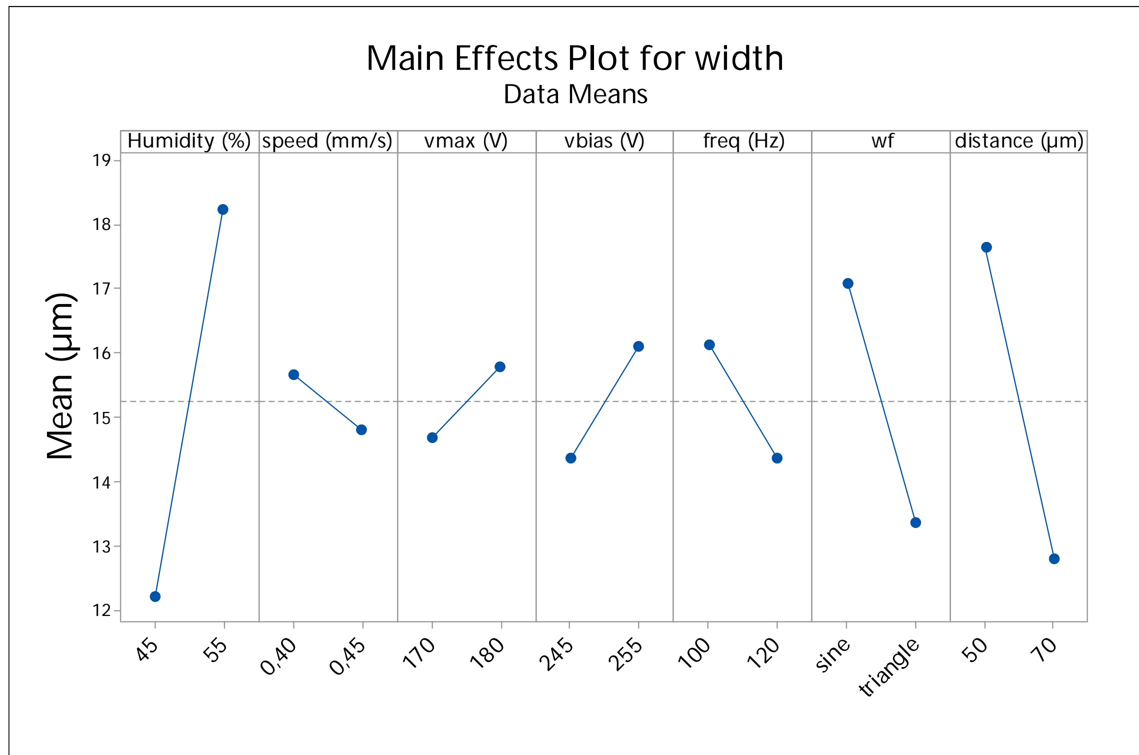

***Figure 26:** Main effects and their strength.*

80.28 % of output variability can be explained by the regression model generated with this data. This is not a very good fit, for example Pekkanen et al. achieved 99.32 % fit when analyzing the parameter effects on droplet velocity of a conventional piezo-inkjet [31]. A possible cause for the model inaccuracy could be the large effect of the only environmental parameter (humidity). This problem is highlighted by the difficulty of humidity control which is cause by the relatively rudimentary hygrometer. For example, the large size of the hygrometer prevents a direct measurement from the substrate surface; it was also noticed that the response time of the unit is quite long.

The purpose of this experiment was to exclude the insignificant parameters from further, high accuracy response surface DoE, but it was found that all the examined parameters have an effect and cant' be thus excluded. However, including all the parameters to the response surface experiment is impossible due to practical limitations.

4.2.2 Response surface model for parameters effects

The humidity had to be excluded from further testing in order to do the experiment in a reasonable amount of time. This meant that the experiments were done in room humidity which was measured to be 45 % with a variation of 0 %-units. However, as mentioned in previous chapter, the response time of hygrometer unit is limited, so possible changes might have happened undetected. Additional simplification was the exclusion of the only categorical parameter: all the measurements were done using sine wave

form. This left V_{max}, V_{bias}, frequency, printing speed and nozzle-to-substrate distance as the remaining inputs.

Central composite response surface design was chosen so that possible quadratic effects (i.e. curvature of the response plane) could be detected by the model. The design accomplishes this by including more parameter levels in the design; specifically, axial and center points are taken into account as well as the cube corner points. The chosen design for these five factors consisted of 108 runs including the replicate. The number of cube points was 64, cube center points 16, axial points 20 and axial center points 8. The alpha value, which determines the high and low parameter values, was 2,366. A description of all the runs with corresponding output measurements is given in Appendix B.

Analysis of variance (ANOVA) was used to separate significant and insignificant inputs and to determine the strength of effects. Interesting statistical parameters here are the P- and F-values. P-value of under 0.05 means that there is enough statistical evidence to reject the null hypothesis which claims that the observed output variation is caused by something else than the input parameter. The magnitude of the F-value signifies the strength of the effect. The insignificant parameters were removed gradually based on the P-values. However, before analyzing the ANOVA-results, the model validity was checked by looking at the randomness and normality of the residual distribution.

First, unusual observations were diagnosed. Seven were found. Two of these were due to bad measurements; the other five could not be accounted for. The unusual observations are shown in Figure 27 which plots the deviation of the observed width from the width predicted by the model (residual) against the observation order. It seems that all unusual observations occurred in two subsequent blocks. It is improbable that the humidity could change so rapidly. Gradual clogging of the nozzle and subsequent detachment of the obstacle might cause this type of behavior. It has also been noticed that the nozzle tip starts to wet during printing from the outside and ink droplet forms. Since the droplet decreases the jetting rate by delocalizing the electric field, gradual droplet formation and sudden detachment of the droplet might cause a similar effect. However, since it it’s not clear what is causing the effect the outliers can’t be excluded from the data. Otherwise the data seems to be randomly distributed.

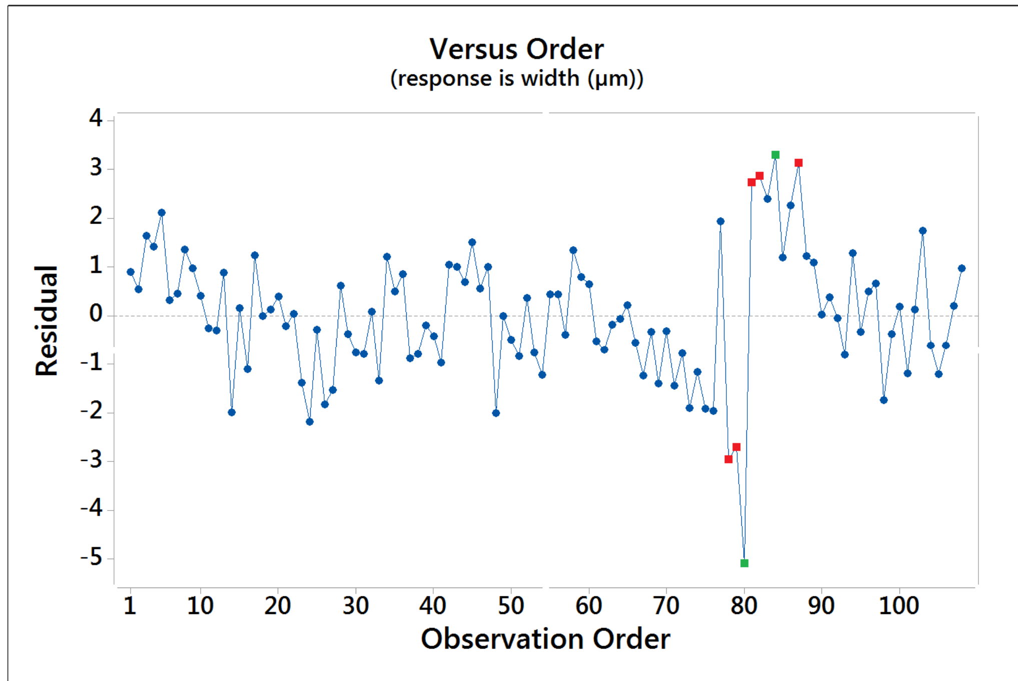

Figure 27: *Unusual observations. Green are due to measurement error; red could not be accounted for.*

The normality of the distribution was checked using the histogram of residual shown in Figure 28. The residuals seem to follow the fitted curve of normal distribution quite well. Therefore, it can be concluded that the model is valid.

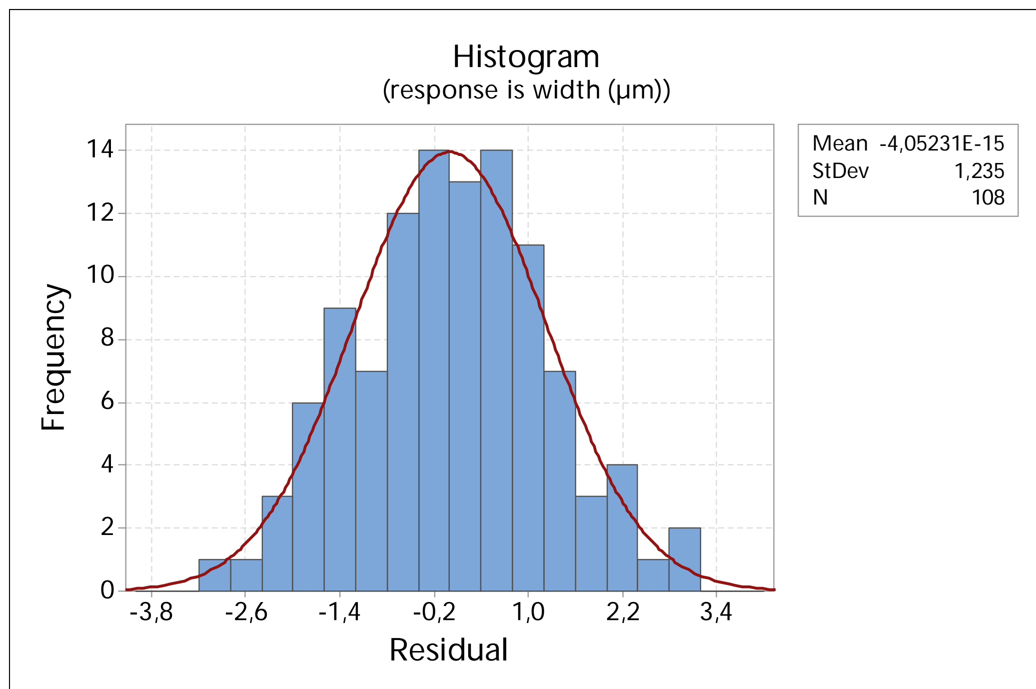

Figure 28: *Histogram of residual vs. the observation frequency. The fitted curve follows normal distribution.*

The final ANOVA-results are shown in Figure 29.

Analysis of Variance

Source	DF	Adj SS	Adj MS	F-Value	P-Value
Model	11	2062,84	187,531	110,37	0,000
Blocks	3	262,96	87,655	51,59	0,000
Linear	5	1726,29	345,258	203,21	0,000
vmax (V)	1	76,31	76,308	44,91	0,000
vbias (V)	1	251,71	251,709	148,15	0,000
freq (Hz)	1	424,16	424,160	249,65	0,000
speed (mm/s)	1	9,13	9,131	5,37	0,023
distance (µm)	1	964,98	964,980	567,95	0,000
Square	1	50,57	50,572	29,77	0,000
distance (µm)*distance (µm)	1	50,57	50,572	29,77	0,000
2-Way Interaction	2	23,01	11,503	6,77	0,002
vmax (V)*vbias (V)	1	13,68	13,685	8,05	0,006
vmax (V)*freq (Hz)	1	9,32	9,321	5,49	0,021
Error	96	163,11	1,699		
Lack-of-Fit	76	125,36	1,649	0,87	0,674
Pure Error	20	37,75	1,888		
Total	107	2225,95			

Figure 29: *Data for analysis of variance (ANOVA) results for response surface design.*

If the parameters are sorted by their respective F-values, it is clear that they follow the same order as the one found in the previous factorial design. The nozzle-to-substrate distance has the most significant effect followed by frequency, V_{bias}, V_{max} and printing speed. The P-values also suggest that $V_{max} * V_{bias}$ and $V_{max} * frequency$ -interactions and the quadratic term of the nozzle-to-substrate distance are significant. The strength and direction of the main effects can be seen in Figure 30.

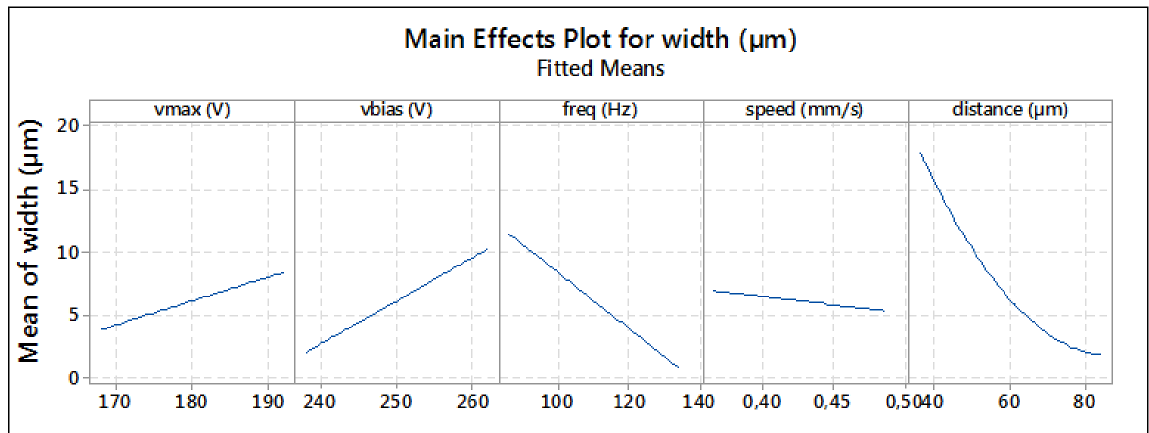

Figure 30: *Main effects plot for width. The effect of nozzle-to-substrate distance is quadratic.*

The quadratic effect of nozzle-to-substrate distance can be understood by recalling the Coloumb's law of force interaction between point charges:

$$|\boldsymbol{F}| = k_e \frac{|q_1 q_2|}{r^2}, \tag{8}$$

where $\boldsymbol{F}$ is the force, k_e the Coulomb's constant, q the charge and r the distance between the charges. The force can be seen to be inversely proportional to the square of the distance. Although Coulombs law is derived for point charges, a similar relation should hold for the SIJ as well: the force acting on the charged ink meniscus at the nozzle tip is inversely proportional to the nozzle-to-substrate distance squared. This would also explain why the effect is the strongest one recorded. Explanation for other parameter effects was given in Table 6.

The effects of interaction terms are shown in Figure 31. The effect of V_{max} depends on V_{bias} or frequency value in which it is measured. For example, a 20 Volt increase in V_{max} increases the conductor width more if V_{bias} value is high compared to when it is low; for frequency the relationship is opposite.

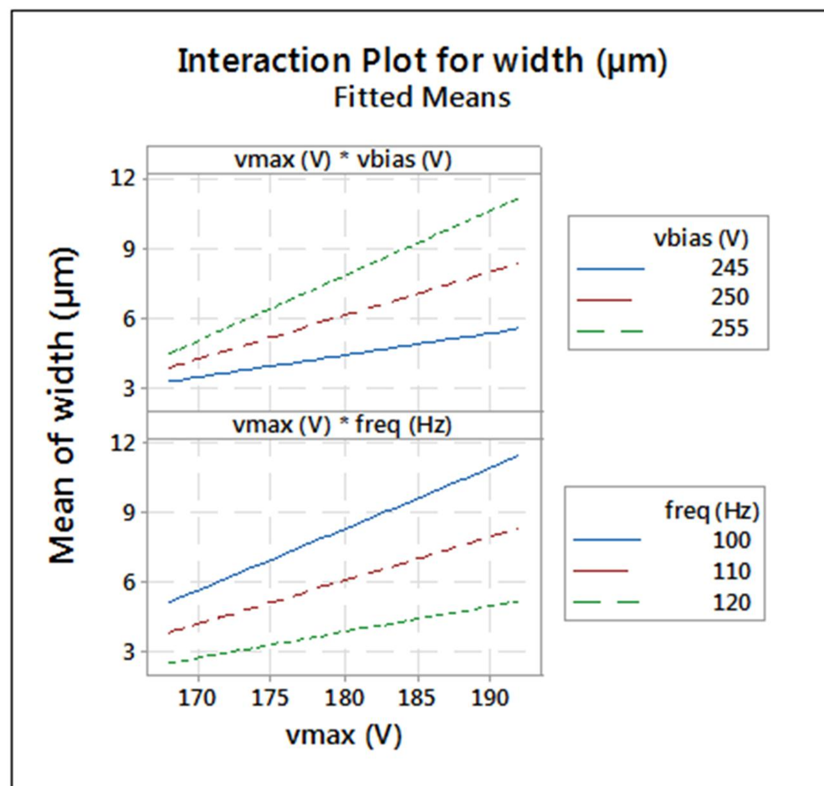

Figure 31: *Effects of parameter interactions.*

Regression analysis was used to relate the width to the input parameters in one simple equation:

$$width(\mu m) = \mathbf{641} - \mathbf{3.6}A - \mathbf{2.99}B + \mathbf{1.152}C + \mathbf{13.00}D - \mathbf{1.112}E + \mathbf{0.00649}D^2 + \mathbf{0.01850}AB - \mathbf{0.00763}AC, \quad (9)$$

where A, B, C, D and E are the V_{max} (V), V_{bias} (V), frequency (Hz), speed (mm/sec) and nozzle-to-substrate distance (µm), respectively. Statistical analysis shows that this model explains 90.79% of the width variation. This is quite good result.

However, the Equation (9) is applicable only in relative humidity of 45% when a sine wave, standard nozzle and oxygen plasma cleaned Ti/W-coated silicon substrate is used. If the nozzle or the substrate is changed or if there is a long time interval between printing runs, a re-calibration has to be done. This means that the first term on the right hand side of the equation ("641") has to be determined. The easiest way to do this is to print a zig-zag pattern with predetermined conductor pitch (say 6 µm for 5 µm target width) and vary the parameters until the conductors can be seen as separate through the side view camera.

Because of the restricted applicability of the model, the important lesson of this chapter is not the regression equation but the identification of significant predictor parameters and the direction and the magnitude of their respective effects.

4.3 Conductor topography and resistance

Depending on wetting characteristics of the substrate, thickness of sintered conductors can be as low as 10% of their width. In the case of a 5 micron conductor this would translate to a thickness of ~50 nanometers. Such at thin "conductor" is not conductive at all. Therefore, a multilayer approach to printing the conductors has to be taken. This means that the layer count vs. thickness and thickness vs. resistance –relationships have to be investigated.

The results shown in this chapter were obtained with super fine nozzle, silver ink NPS-J and silicon substrate with 2 micron silicon oxide on top. Conductors with two and five micron target width were printed with various layer counts. However, the true width of the conductors varied significantly. The test pattern was a four point structure shown in Figure 32. Test and printing parameters are shown in Table 7.

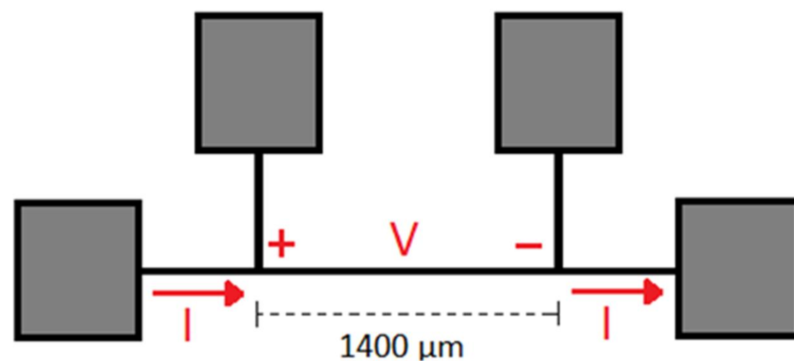

Figure 32: *Four point test pattern for topographical and resistance measurements.*

***Table 7:** Test and printing parameters for topographical and resistance measurements.*

Parameter	Test A (5 µm target width)	Test B (2 µm target width)
Number of sets	2	1
Number of layers	1-10, 15, 20, 25, 30, 35, 40	10, 15, 20, 25, 30, 35, 40
Vbias (V)	170	160
Vmax (V)	200	186
Waveform	sine	sine
Frequency (Hz)	1000	1000
Printing speed (mm/s)	1	1
Nozzle-to-substrate distance (µm)	30	30
Humidity (%)	40…50	40…50
Temperature (°C)	21.4	22.6

4.3.1 Topography

The topography was measured with atomic force microscope (AFM) XE-100, product of Park Systems Corp., along ten micron length of the conductor. The resulting images were analyzed with image analysis tool XEI, also by Park Systems Corp.

Figure 33 shows enhanced color AFM images of sintered five micron (set 2) samples with different number of layers: a) one, b) five, c) ten and d) fifteen layers. Average cross-sections of these samples are shown in Figure 34.

As expected, the individual layers are very thin. It also seems to be that the first few layers act as a seed layer for the subsequent ones; when the layer number is increased additional ink starts to accumulate to the middle of the conductor increasing the conductor growth rate. This can be explained by the different wetting behavior on top of silicon oxide compared to dry ink. Similar behavior was observed by Sadie et al. for pillar structures fabricated with conventional inkjet. They divided the pillar formation in three regimes: wetting, tapering and growth. This growth mechanism seems to explain the

growth of the SIJ printed conductors as well. See reference [32] for more detailed analysis.

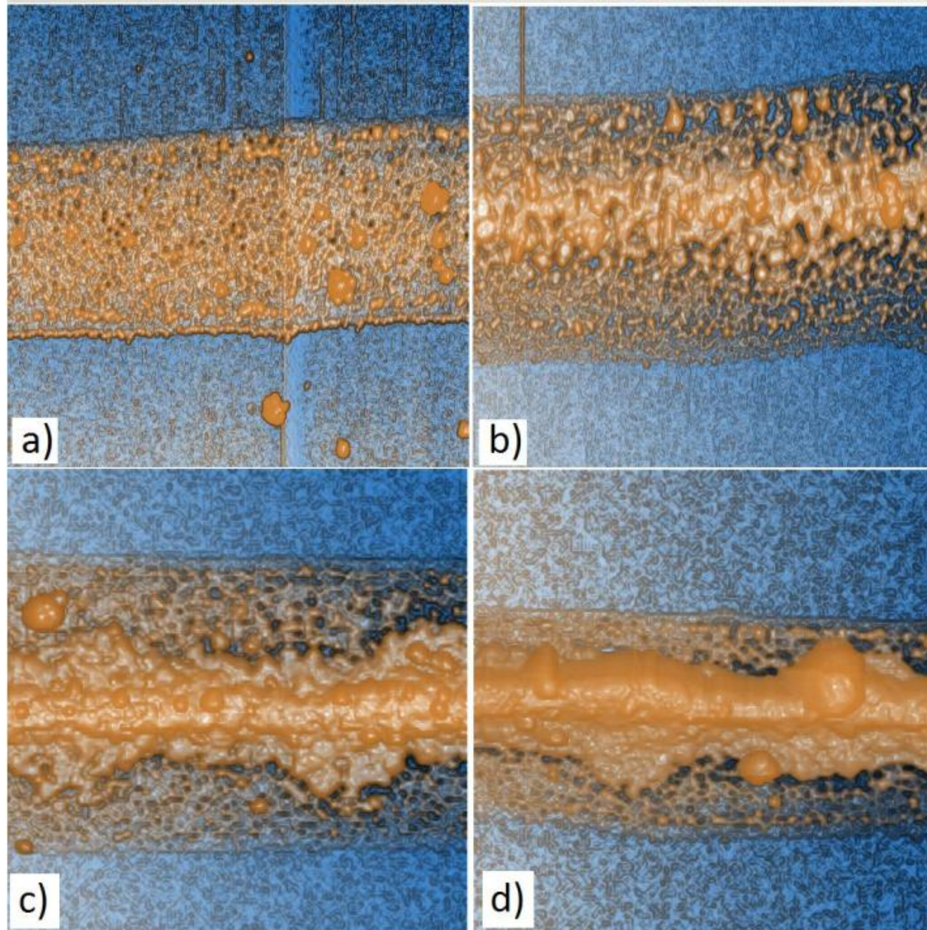

Figure 33: *Enhanced color AFM images of a) 1 layer; b) 5 layer; c) 10 layer and d) 15 layer sintered conductors with 5 micron width. Picture dimensions are 10x10 µm (height x width) except for b) which is 7x10 µm.*

The average peak to valley heights for the conductor cross-sections shown in Figure 34 are 50 nm, 183 nm, 570 nm and 850 nm for the samples (a), (b), (c) and (d), respectively. It is interesting to note that the average peak to valley height of the one layer sample is about one third of the sample with five layers. This could be due to process variation i.e. varying jetting rate (ink flow rate). If the rate would be same in both cases, one would expect the average peak-to-valley height to increase in (at least) 50 nanometer increments resulting in 250 nm thick five layer conductor. However, the width of the conductor is likely to affect the growth rate as well: wider multilayer conductors should grow faster since the ink flow rate is faster. The AFM measurements showed that the five micron target width produced conductors with width ranging from 4.4 to 7.4 micron; for two micron target width the range was 2 to 2.8 micron. This means that the width and layer count could be used as predictors when generating a statistical model for the conductor thickness.

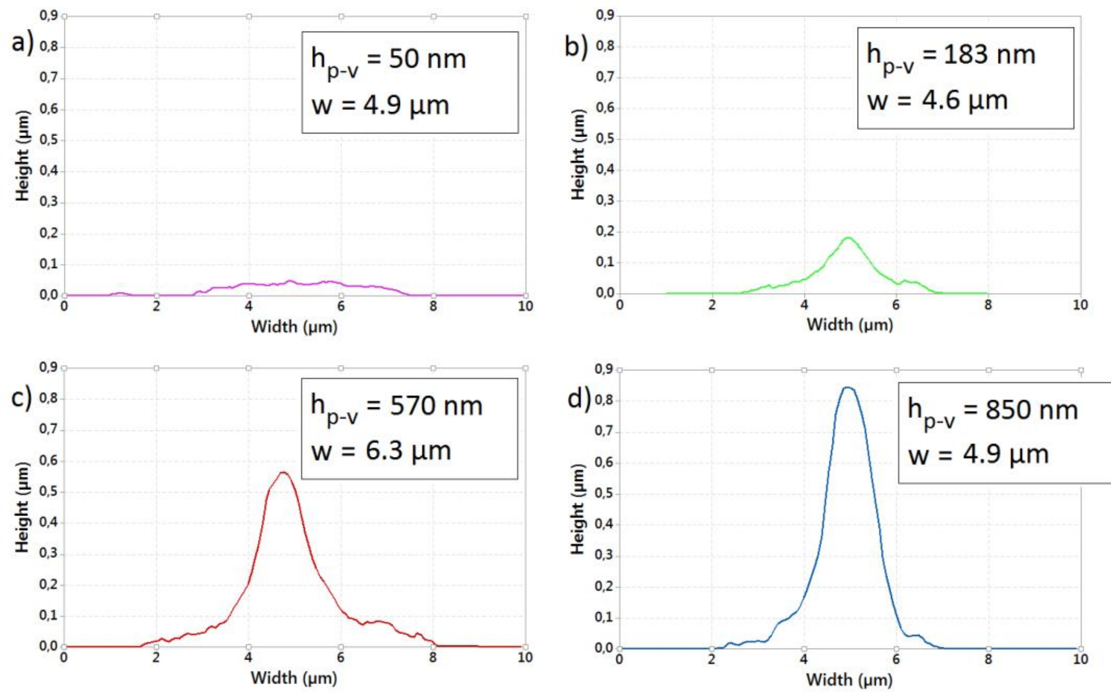

Figure 34: *Average topography of samples shown in Figure 33: a) 1; b) 5; c) 10 and d) 15 layers. h(p-v) stands for peak-to-valley height and w for width.*

A custom response surface design was used to analyze the effect of width and layer count on the thickness. The design was based on the thickness vs. layer count data shown in Figure 35 and the exact width measurements for each data point.

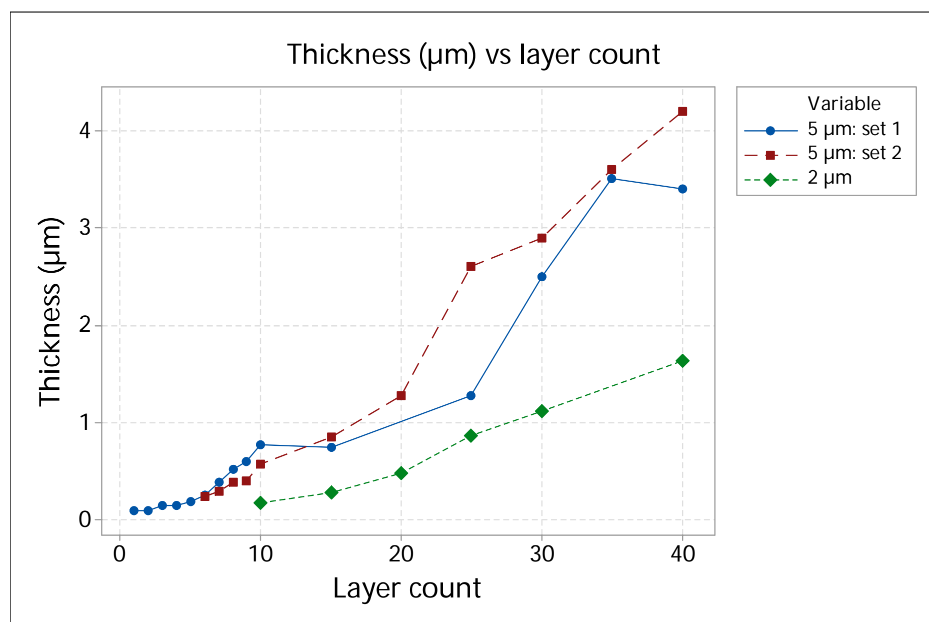

Figure 35: *Thickness vs. layer count.*

The validity of the model was checked using residual plots shown in Figure 36. The residuals have to be both normally and randomly distributed for the model to be valid. Slight oscillation of residuals can be seen in the normal probability plot, but the Ander-

son-Darling test (P-value > 0.05) shows that the distribution is indeed normal. Also the histogram seems to support this conclusion. However, the "versus fits" plot shows that the variance of the error is not constant; the spread of the error is larger at smaller fitted values compared to larger ones. This could indicate that the data is not valid even though the normality requirement is fulfilled.

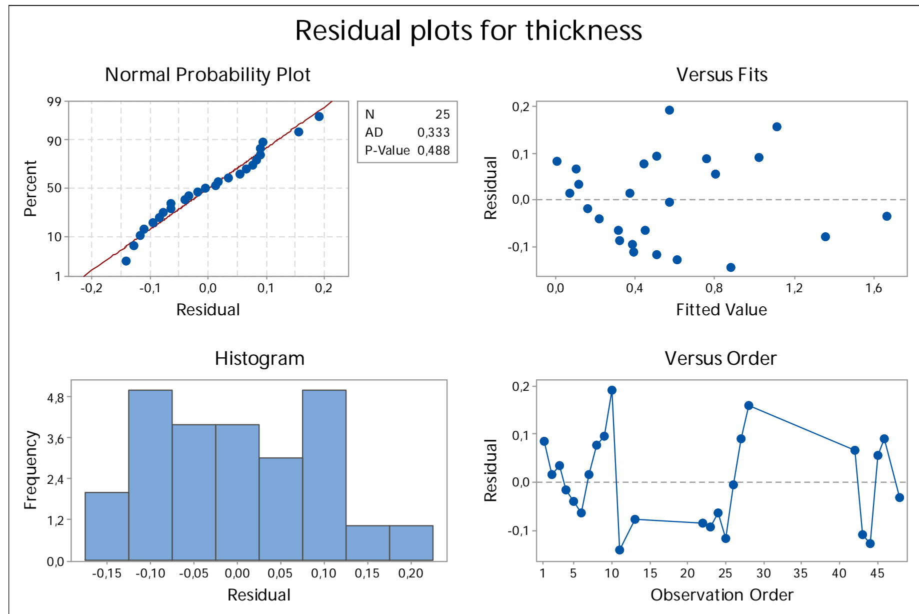

Figure 36: *Residual plots for thickness vs. the model.*

In order to make the residual behave better, the response data must be transformed. Box-Cox procedure was used to determine the most suitable transformation. The results of the analysis are shown in Figure 37.

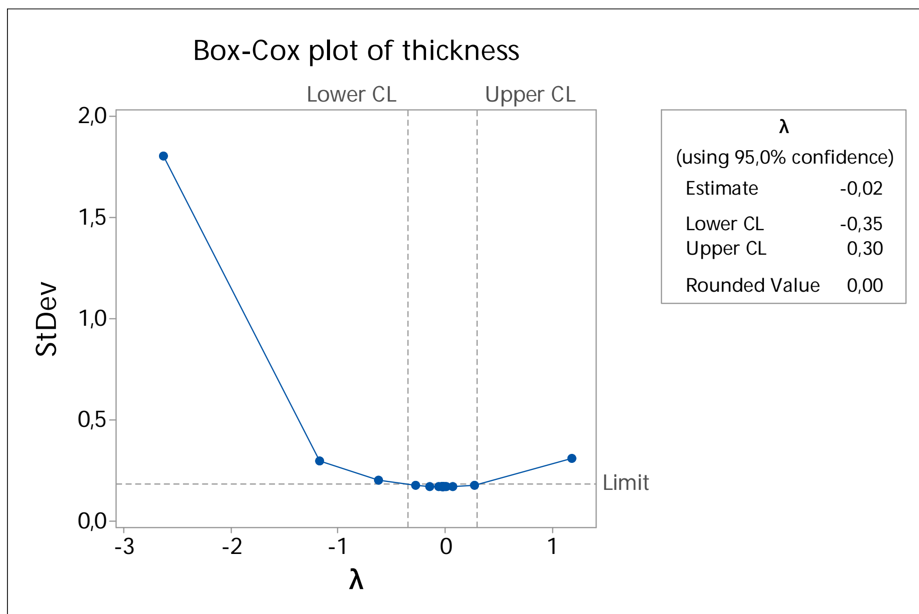

Figure 37: *Box-Cox plot for determining the most suitable data transformation function for the response variable (conductor thickness).*

The suitable transformation function in Box-Cox procedure is indicated by the lambda value; for example, for $\lambda = 0.5$ the function is square root and for $\lambda = 0$ natural logarithm. The estimated λ for this data set is -0.02 which rounds up to $\lambda = 0$. Thus, the following equation should be used for data transformation:

$$X_t = \ln(X_o), \tag{10}$$

where X_t is the transformed value and X_o the original value of the data point.

A custom response surface design was repeated for the transformed data. Two unusual observations were detected. One of these was due to error in the printing process (jetting stopped during printing); the other one could not be accounted for. Again, the validity of the model was checked using the residual plots. These are shown in Figure 38.

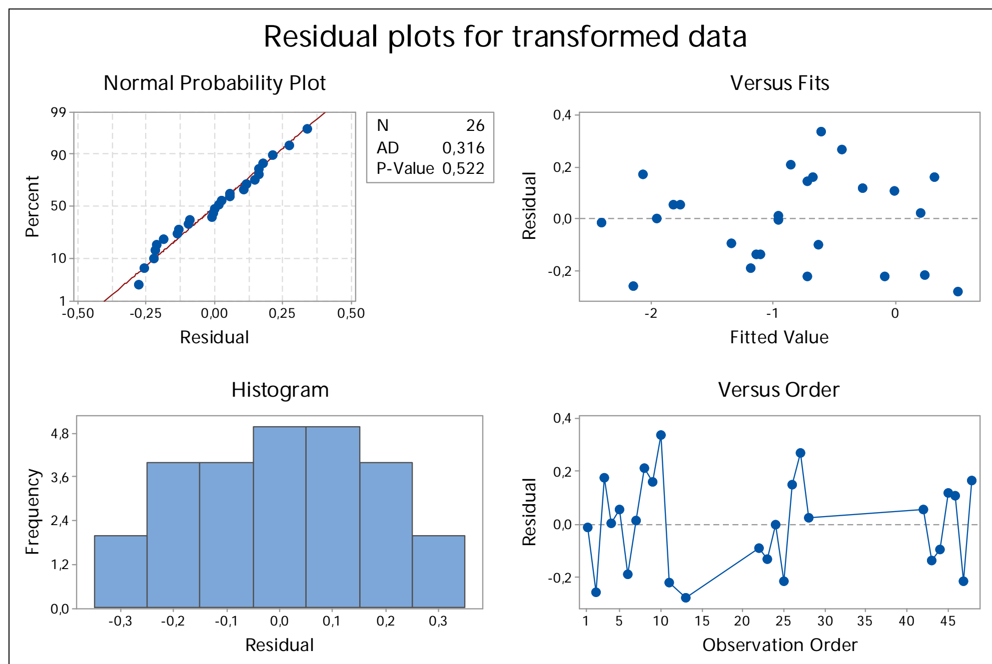

Figure 38: *Residual plots for thickness after the data transformation.*

Same as before, the residuals seem normally distributed. However, in this case the requirement of random distribution is filled as well. This can be seen from the “versus fits” plot where the variance of the residual remains constant regardless of magnitude of the fitted value. Thus, the model is valid.

Insignificant predictors/predictor combinations were removed from the model based on the P-value. The resulting data for ANOVA is shown in Figure 39. According to the F-values, the layer count seems to be the dominating predictor followed by width. Additionally, the effect of the layer count is quadratic.

```
Analysis of Variance

Source                       DF   Adj SS   Adj MS  F-Value  P-Value
Model                         5  16,7887  3,35773    89,72    0,000
  Blocks                      2   0,0328  0,01639     0,44    0,651
  Linear                      2  10,7163  5,35813   143,17    0,000
    Layer count               1   9,6416  9,64163   257,62    0,000
    Width                     1   0,7027  0,70270    18,78    0,000
  Square                      1   1,5428  1,54280    41,22    0,000
    Layer count*Layer count   1   1,5428  1,54280    41,22    0,000
Error                        20   0,7485  0,03743
Total                        25  17,5372
```

Figure 39: *Data for ANOVA-results.*

The following regression equation for conductor thickness was generated based on the data:

$$thickness\ (\mu m) = e\hat{}(-3.912 + 0.1797A + 0.2801B - 0.002324A^2) \qquad (11)$$

where A and B are the layer count and width (µm), respectively. This model explains 95.54% of the thickness variation. This is a relatively good result, but the model has other limitations because it is based purely on statistics and doesn't take physical phenomena into account. The limitations become apparent from Figure 40 which plots the equation (11) for two, five and six micron wide conductors.

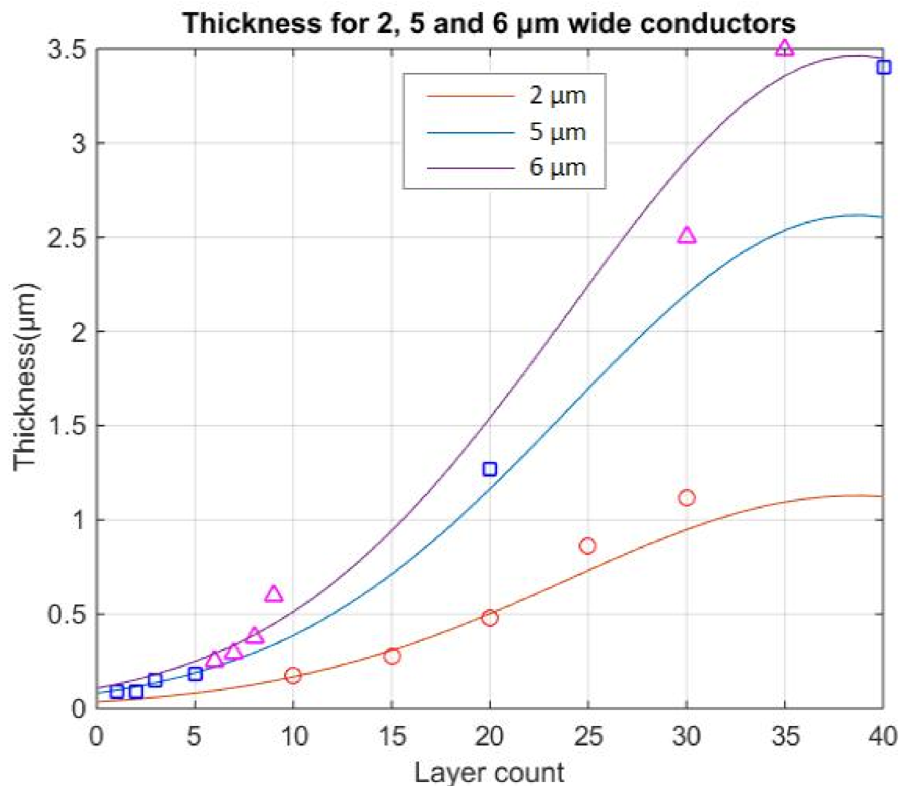

Figure 40: *Thickness for 2, 5 and 6 µm wide conductor as predicted by equation (11). The markers are for conductors with approximately two (circle), five (square) and six µm (triangle) width.*

There seems to be an upper limit to applying the model. Since the quadratic term of the layer count is negative, at certain value it will become larger than the sum of the linear terms. In other words, according to the model, at certain layer count the thickness of the conductor starts to decrease although the number of layers is increased; based on Figure 40, this happens after 39 layers. In reality, this is of course impossible. It also seems that the model predicts a finite thickness for zero layers - impossible as well. Therefore, equation (11) is only valid when the layer count is equal to or larger than one. However, determining an upper limit is not that clear cut. The upside to this is that it poses an opportunity to supplement the statistical model with actual physical phenomena.

Sadie et al. noted that the growth rate of piezo-inkjet printed pillars is linear after sufficient number of deposited layers; they also noted that the linear region coincides with the fastest growth rate [32]. It is assumed here, that the growth behavior is similar in the case of SIJ. This means that the threshold layer count for linear growth can be estimated by finding the maximum derivative of equation (11). Figure 41 plots the derivative for two and five micron wide conductors.

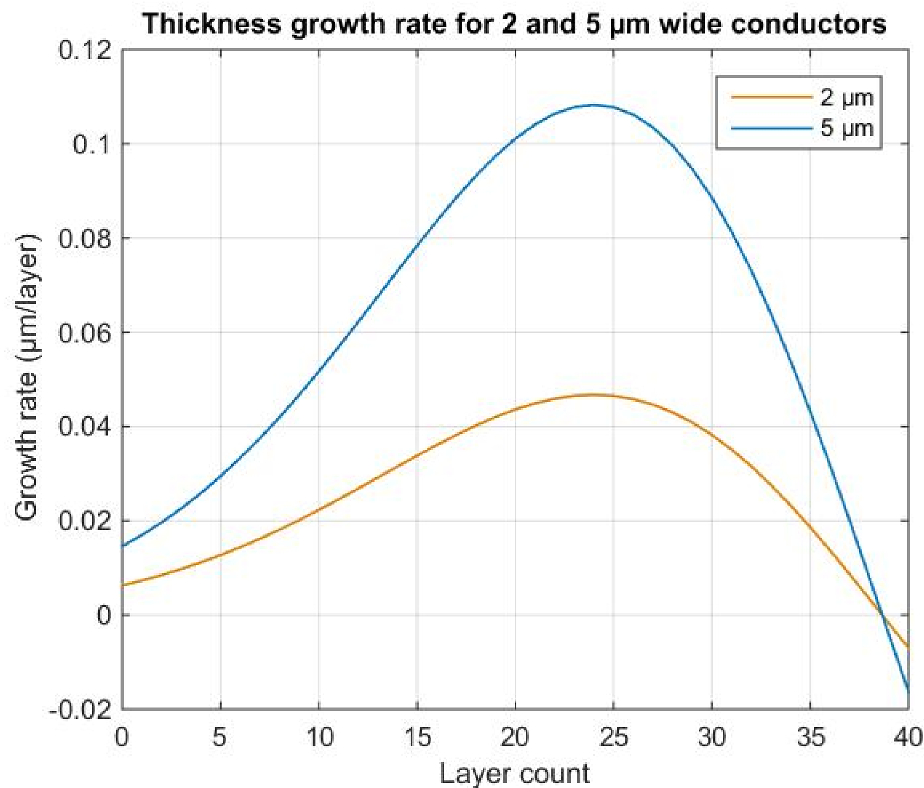

Figure 41: *Growth rate vs layer count for 2 and 5 micron wide conductors.*

It is clear from Figure 41 that the fastest growth rate occurs at 24 layers regardless of the conductor width. In other words, equation (11) is applicable only when $1 \leq layer\ count \leq \mathbf{24}$. When $layer\ count > \mathbf{24}$, the growth is linear and happens at maximum growth rate. Thickness can be then approximated by equation (12):

$$thickness\ (\mu m) = t(\mathbf{24}, B) + \left[\frac{d}{dA} t(A, B)\right]_{A=24} * (A - \mathbf{24}), \quad (12)$$

where $t(A, B)$ is equation (11), A layer count and B conductor width. Figure 42 shows this correction for 2 and 5 micron wide conductors.

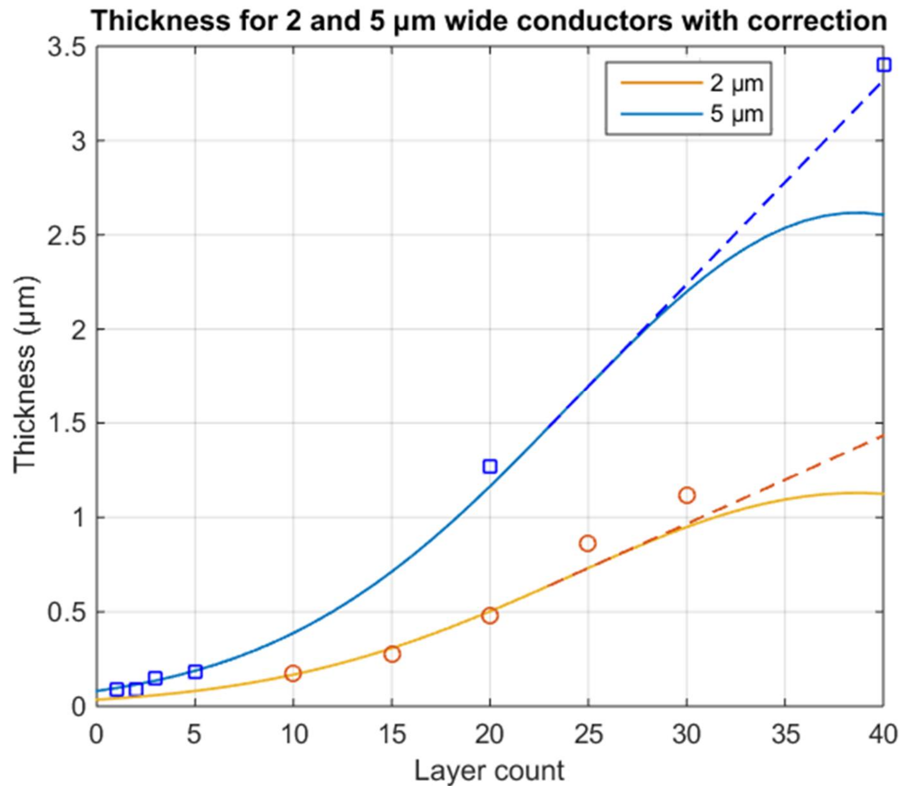

Figure 42: *Thickness vs. layer count for 2 and 5 µm conductors. The dashed line marks the correction made using equation 12 for layer counts larger than 24. Markers show thicknesses for approximately two (circle) and five µm (square) wide conductors.*

According to Figure 43, it seems that the correction (equation 12, dashed line) predicts the larger values somewhat better than the original model (equation 11, solid line). However, some issues still remain. For example, it has been noted that with some inks the ink flow rate decreases during the printing. This would cause the growth rate to deviate from the linear approximation. In order to validate the model, more data points are needed at larger layer counts.

In conclusion, equation (11) is valid for layer counts 1 to 24 and equation (12) for larger layer counts if the growth rate remains linear after hitting the maximum.

4.3.2 Resistance

The conductor resistance was measured using Keithley 2400 Multimeter and purpose built probe station shown in Figure 44. The measurement procedure is such that a constant current is fed through a certain length of a conductor and the voltage drop over that

part is measured (see Figure 32). The multimeter automatically converts the measurement to a resistance value. Using four point instead of two point resistance measurement increases the measurement accuracy by disposing the error caused by measurement setup (lossy probe leads etc.).

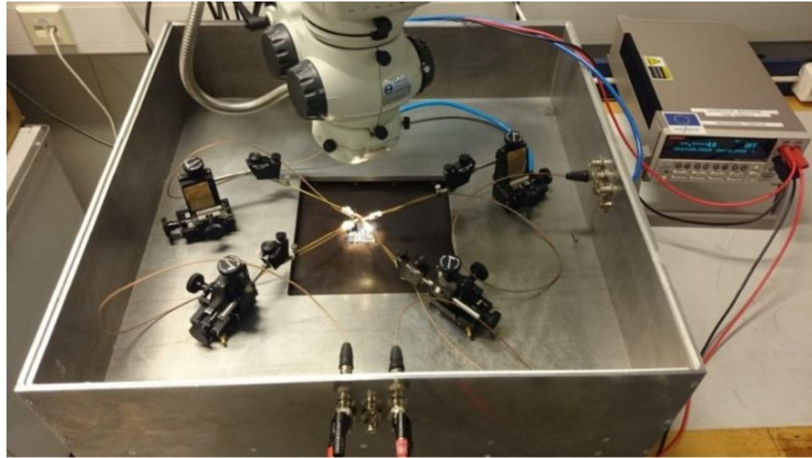

Figure 44: *Keithley 2400 multimeter and probe station for four point measurements.*

It is common practice to convert the resistance to sheet resistance values. This is done by dividing the measured resistance R by the number of squares the conductor consists of. The latter equals simply the length L of the conductor divided by its width W [31]:

$$R_{sheet} = \frac{R}{L/W} \tag{12}$$

This can be converted to resistivity value if the thickness t of the conductor is known [33]:

$$\rho = R_{sheet} * t = \frac{Rt}{L/W} \tag{13}$$

The results for sheet resistance measurements are shown in Figure 45; as expected the sheet resistance decreases exponentially as conductor thickness is increased. Together with the measured peak-to-valley thicknesses, these values were used to calculate the resistivity of the conductors. The average resistivity value for Test A was 17 µOhm·cm and 15 µOhm·cm for Test B. The deviation from the ink datasheet value of 3 µOhm·cm [22] can be explained by the somewhat unusual topography of the conductors. Sheet resistance based determination of resistivity applies best for conductors with approximately rectangular profile, but as shown in Figure 34, the profile of the printed conductors is shaped like a bell curve. It is also probable that a substantial part of the line is non-conductive, the conductivity taking place in the center where most material is accumulated instead of the edges with less material (see Figure 33). Because the measured line width takes account of this non-conductive part as well, the calculated resistivity values end up higher than the true resistivity.

Better approximation of resistivity can be obtained if the conductor cross-sectional area A_{cross} is known; in this case equation (13) can be replaced by $\rho = R * A_{cross}/L$. A_{cross} was determined for the sample conductors using numerical integration of AFM topography images. This approach yielded an average resistivity value of 4.9 µOhm·cm which compares much more favorably to the ink datasheet value of 3 µOhm·cm [22] or bulk silver resistivity of 1.59 µOhm·cm [9]. This means that the quality of the sintered nanoparticle structure is not affected negatively by the EHD printing process. It is also important to note that the multilayer printing with conventional DoD will result in similar non-rectangular conductor profile [32] and higher conductor resistivity if the calculation is based on sheet resistance instead of cross-sectional area.

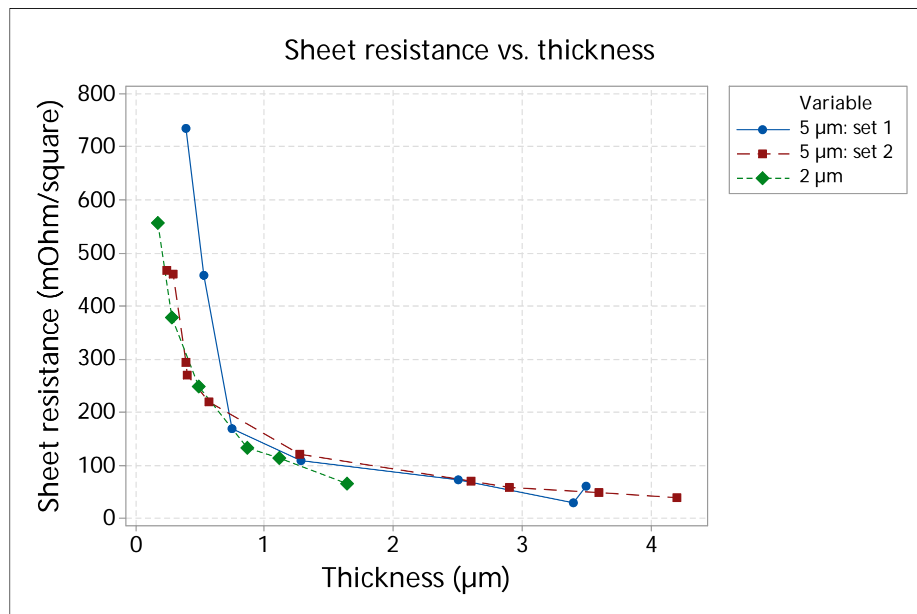

Figure 45: *Sheet resistance vs. thickness for 5 µm and 2 µm wide conductors.*

Nevertheless, a statistical model was derived to predict the sheet resistance values. Since sheet resistance already contains the information about conductor width, thickness could be used as the only predictor. A simple nonlinear regression was used to approximate the relationship between response and predictor. This required an expectation function to be determined. Based on Figure 45, exponential function of the form $A * thickness^{\wedge}B$ was chosen as the best approximation.

A model was generated based on the expectation function and its validity was checked using the residual plots. It was found that the distribution is non-normal. Again, the Box-Cox procedure was used to detect the best function for normalizing data. $\lambda = -0.04$ was returned by the BC-procedure indicating natural logarithm as the most suitable function. Based on this, the response data was transformed using Equation 10.

The residual plots for the transformed data are shown in Figure 46. According to the Anderson-Darling statistics in the inset of the “Normal Probability Plot”, the trans-

formed data follows a normal distribution. However, it does this only barely since the critical P-value for rejecting the null hypothesis of normally distributed data is < 0.05. The histogram of residuals seems to follow normal distribution as well. The requirement for constant variance of residual over all fitted values seems to be also fulfilled. In conclusion, the data has some issues but seems to be nevertheless good enough for a valid model.

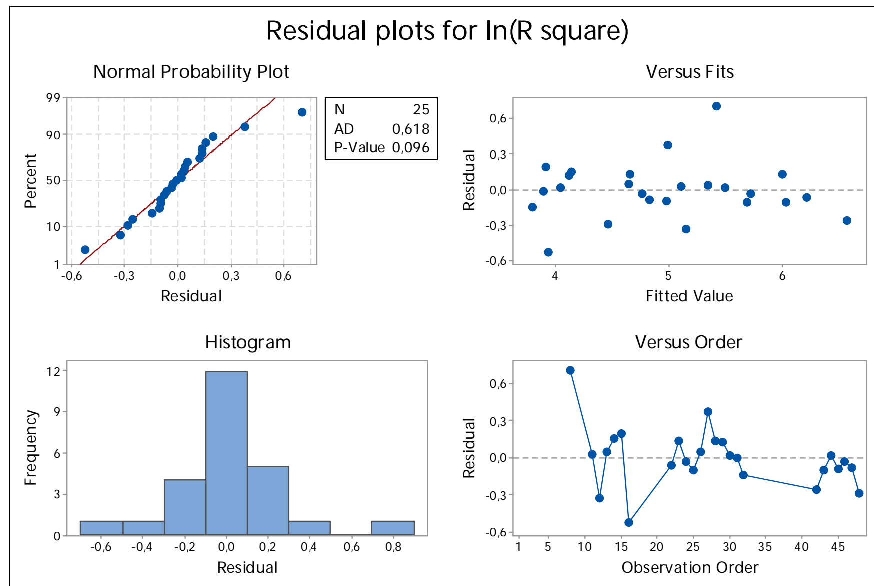

Figure 46: *Residual plots for the transformed data.*

The resulting model for the transformed data is shown in Figure 47.

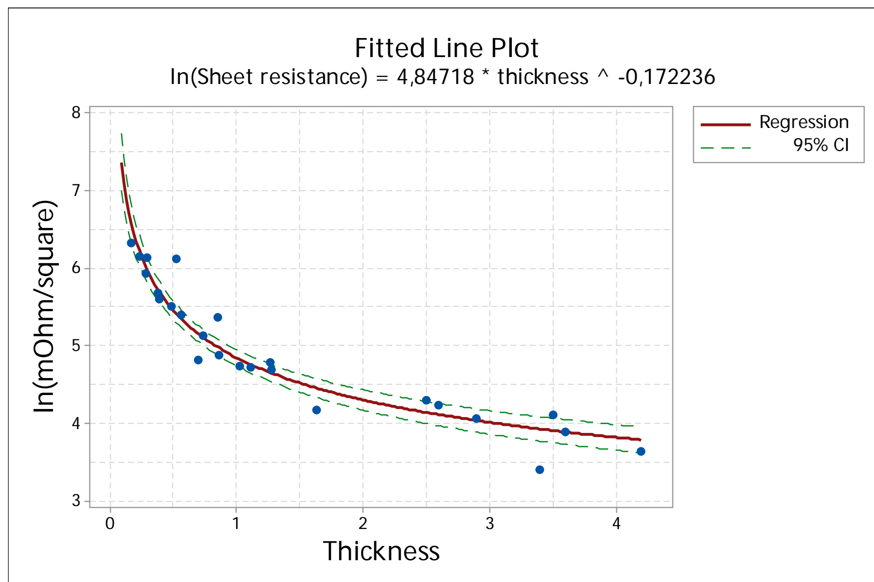

Figure 47: *Model for the transformed data.*

In Figure 47 the green dashed lines indicate the 95% confidence interval for the model. Some outliers still exist, especially at small thicknesses, but most data points are within

the interval. According to R-squared value the model predicts 92.2% of response variation.

The regression equation shown in Figure 47 can be transformed back to original scale by simply taking the antilog of natural logarithm:

$$Sheet\ resistance\ (mOhm/square) = e\verb|^|(4{,}84718A^{-0{,}172236}) \quad (14)$$

where A is thickness of the conductor in µm. The regression curve is compared to the measured values in Figure 48. Model fit seems to be quite good, but it might be possible to improve the fit even further by using sheet conductance instead of sheet resistance as the output. This might improve the model fit at smaller thicknesses.

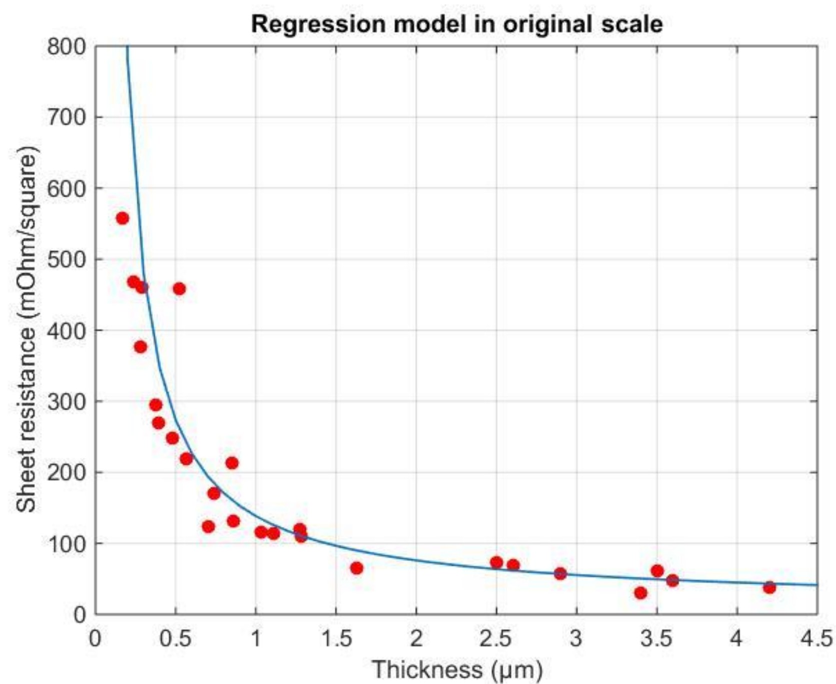

Figure 48: *Equation (14) plotted against the measured sheet resistance values.*

5. RDL DEMONSTRATORS

In previous chapter it was shown that the width, thickness and resistance of the conductors can be controlled. It was also shown, that the conductor widths are small enough for high density wiring applications. However, there is more to manufacturing a high density RDL than conductor width and resistance control. For example, the print quality has to be such that no short circuiting will happen despite the small spacing between the conductors; it is also important that no open circuits occur despite long conductors.

5.1 Designs

Two structures were used to demonstrate the different aspects of the high density RDL. A meander structure shown in Figure 49 was used to show that no open circuits exist even if the length of the conductor is very long. Five and ten micron conductor widths were demonstrated with five and ten micron spacing, respectively. Open circuits can be detected by measuring the resistance between the pads.

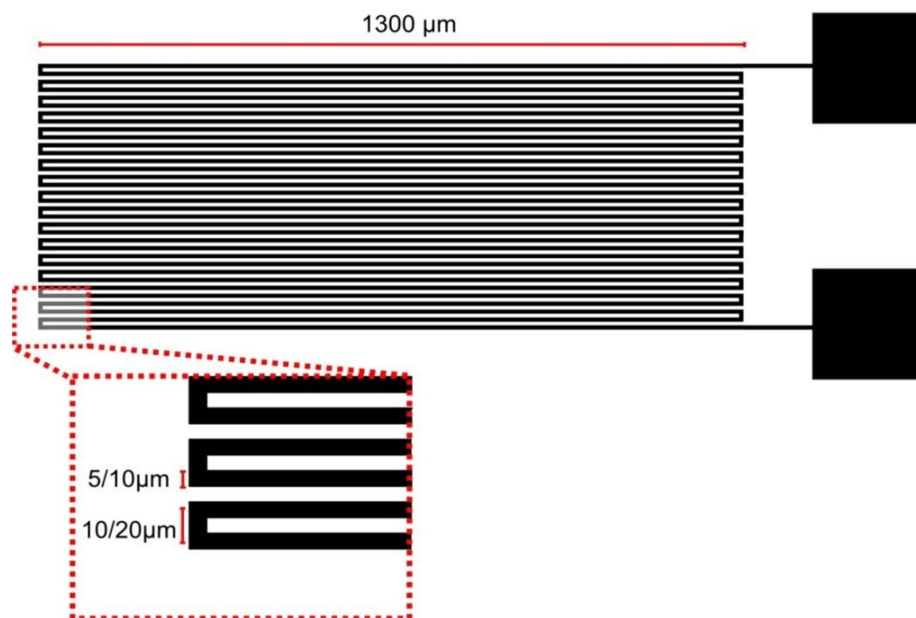

Figure 49: *Meander pattern for open circuit testing.*

A finger structure shown in Figure 50 was used for detecting short circuits. This was also done with 5 and 10 micron conductor widths and spacing. Again, measuring the resistance between the pads should provide proof that no short circuits exist.

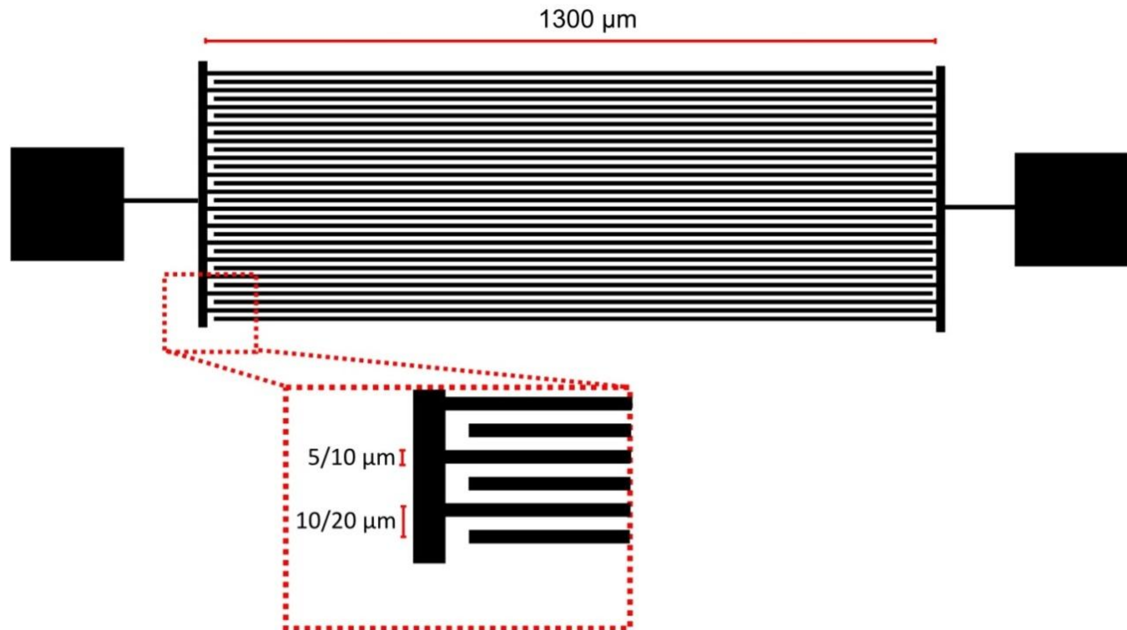

Figure 50: *Finger pattern for short circuit testing.*

The finger structure can also be used to measure the RF-characteristics of the conductors. In this case, however, such measurements were left for later time.

5.2 Demonstrators

Two demonstrators were printed with each width/spacing combination. Visual inspection was done with optical microscope and thickness of the conductors was measured using Wyko NT1100 optical profilometer. The structures were sent out of house for etching and resistance measurements.

Figure 51 shows a part of the finger structure with 5 micron conductor width and spacing. Some thickness variation between the conductors can be seen; the alignment has shifted to right between the upper and lower parts of the structure and there seems to be additional spreading of ink at the tips of the conductors. This puddle formation can be understood if the nozzle movement during printing is considered. As the nozzle comes closer to the end of the conductor, it starts to slow down and before it turns back, it has to stop completely. However, the ink flow rate remains constant so that more material is deposited at the end of the conductors. Similar puddles can be seen every time the printing changes direction. This effect can be seen in all the structures regardless of the ink or other printing parameters.

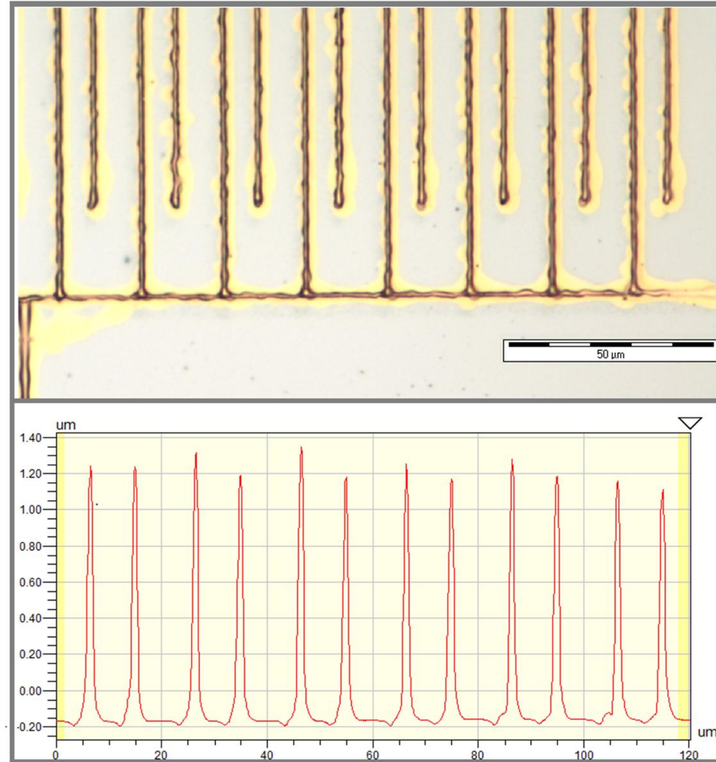

Figure 51: *Finger structure with five micron conductor width/spacing. Note that the topographical graph shows the substrate surface at -0.20 µm.*

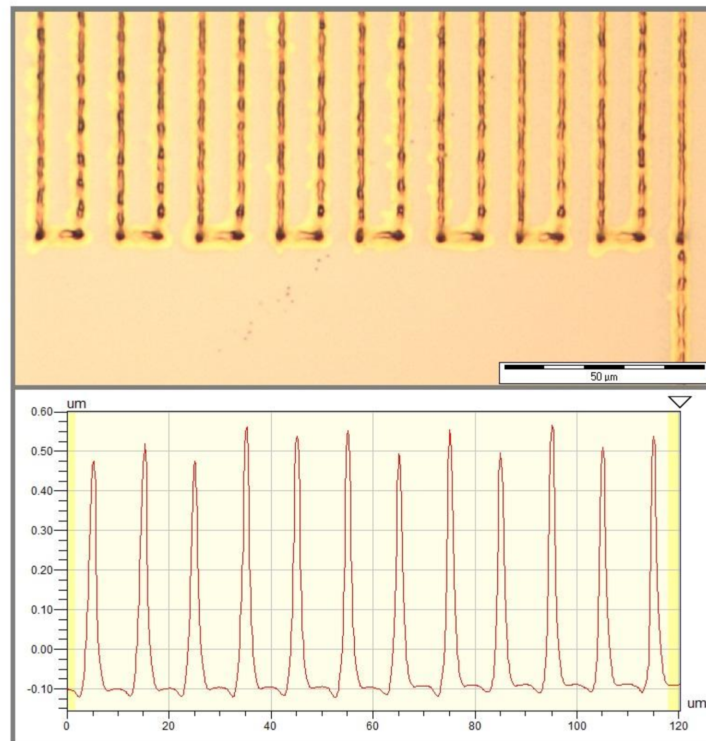

Figure 52: *Meander structure with five micron conductor width/spacing.*

An example of five micron width/spacing meander pattern is shown in Figure 52. Puddle formation is again visible at points where the printing changes direction. At the corners of the meander pattern the printing direction changes twice in a short distance of only ten microns. This causes the puddles to merge. Additionally, a slight oscillation of conductor thickness can be detected from the microscope image. This was also verified with the optical profilometer.

Despite the anomalies, the resistance measurements showed that the finger structures had no short circuits and the meander pattern contained no open circuits.

6. CONCLUSIONS AND FUTURE WORK

The objective of this thesis was to find out if the SIJ could be used in fabrication of a certain part of MEMS package, the redistribution layer (RDL). In order to show that this is indeed possible, statistical models were generated for conductor width, thickness and sheet resistance; additionally, high density conductor structures were printed for short and open circuit testing to demonstrate high density printing capabilities of the SIJ. The main results and regression equations are reiterated here.

It seems that humidity, printing speed, peak and bias voltage, frequency, waveform and nozzle-to-substrate distance all have significant effect on conductor width with humidity and nozzle-to-substrate distance dominating the parameter effects. Further analysis resulted in the following model:

$$width(\mu m) = 641 - 3.6A - 2.99B + 1.152C + 13.00D - 1.112E + 0.00649D^2 + 0.01850AB - 0.00763AC, \quad (9)$$

where A, B, C, D and E are the V_{max} (V), V_{bias} (V), frequency (Hz), speed (mm/sec) and nozzle-to-substrate distance (µm), respectively. This model explains approximately 91% of the width variation. Further analysis showed that the increasing the voltage terms (V_{max} and V_{bias}) increases the conductor width, increasing frequency decreases the width, increasing the printing speed decreases the width and increasing the nozzle-to-substrate distance decreases the width; it was also found out that the effect of V_{max} depends on the V_{bias} and frequency value in which it is measured.

Topography analysis of the conductors showed that their cross-sections are non-rectangular. The thickness growth is therefore slower at beginning and increases until sufficient number of layers have been printed. Analysis showed that width together with layer count can be used as predictors for conductor thickness:

$$thickness\ (\mu m) = e\hat{}(-3.912 + 0.1797A + 0.2801B - 0.002324A^2) \quad (11)$$

where A and B are the layer count and width (µm), respectively. This model was able to predict 95.6% percent of the thickness variation. However, it was noticed that this equation is likely valid only from 1 to 24 layers. Based on previous studies done on inkjet printed pillar growth, it was assumed that after 24 layers the growth rate should remain constant and could be therefore estimated by:

$$thickness\ (\mu m) = t(24, B) + \left[\frac{d}{dA} t(A, B)\right]_{A=24} * (A - 24), \quad (12)$$

where $t(A,B)$ is equation (11), A layer count and B conductor width. However, more measurements at larger layer counts are needed to verify equation (12).

Conductor sheet resistance was found to be inversely proportional to thickness:

$$Sheet\ resistance\ (mOhm/square) = e\text{^}(4{,}84718A^{-0{,}172236}), \qquad (14)$$

where A is thickness of the conductor in µm. This model was able to predict 92.2% of the sheet resistance variation. The sheet resistance values were found to be higher than comparable electroplated conductors. This is most likely due to the non-rectangular cross-sections and nanoparticle nature of the conductors. The conductor resistivity had to be calculated using the average cross-sectional area of the conductors since the sheet resistance based resistivity determination applies only for conductors with rectangular cross-sections. The average resistivity was 4.9 µOhm·cm. This is approximately three times higher than the resistivity of bulk silver and 1.5 times higher than the value given by the ink manufacturer.

In addition to providing statistical models for conductor width, thickness and sheet resistance, it was shown that the printing stability is good enough for making high density single layer structures with down to five micron conductor width and spacing. This was done by printing meander and finger patterns for open and short circuit testing, respectively. Although no short or open circuits were detected, it was noticed that the conductor edge roughness is affected by a puddle effect in places where the printing direction changes.

Regarding the future work, the end application calls for a *multilayer* RDL (as discussed in chapters 2.2.2 and 2.2.3). In order to demonstrate this, the high density meander and finger structures should be printed in two layers separated by dielectric. This means that printing of dielectric on top of sintered conductors and printing of second conductive layer on top of the dielectric have to be investigated. It is also important that the RF-characteristics of the conductors be measured since some of the MEMS devices operate at high frequencies.

REFERENCES

[1] M. Gad-el-Hak (ed.), MEMS – Introduction and fundamentals, 2nd edition, 2006, CRC Press, Boca Raton, USA.

[2] K. Suganuma, Introduction to printed electronics, 1st edition, 2014, New York, USA.

[3] I. M. Huchings (ed.), G. D. Marting (ed.), Inkjet technology for digital fabrication, 1st edition, 2013, John Wiley & Sons, Chichester, UK.

[4] K. Murata, US Patent application US7434912 B2 – Ultrafine fluid jet apparatus, 2008.

[5] R. R. Tummala, Fundamentals of microsystems packaging, 2001, McGraw-Hill Professional, USA.

[6] R. R. Tummala, System on package: Miniaturization of the entire system, 2008, McGraw-Hill Professional, USA.

[7] N. Kanani, Electroplating: Basic principles, processes and practices, 2004, Elsevier, Oxford, UK.

[8] M. Töpper, Th. Stolle, H. Reichl, "Low cost electroless copper metallization of BCB for high-density wiring systems", International symposium on advanced packaging materials, pp. 202-208, 1999.

[9] Resistivity and temperature coefficient at 20 C. Available: http://hyperphysics.phy-astr.gsu.edu/hbase/tables/rstiv.html, Visited: 25.09.2015.

[10] K. Henttinen, Handbook of silicon based MEMS materials and technologies – Chapter 39: Via technologies for MEMS, 2010, William Andrew Publishing, Boston, USA.

[11] B. Khorramdel et al, "Inkjet filling of TSVs with silver nanoparticle ink", Proceedings of Electronic System and Technology Conference (ESTC), pp. 1-5, 2014

[12] B. Khorramdel et al, "Metallization of high density TSVs using super inkjet technology", Proceedings of IEEE 65th Electronic Components and Technology Conference (ECTC), pp. 968-972, 2015.

[13] H. Kuisma, Handbook of silicon based MEMS materials and technologies – Chapter 30: Introduction to encapsulation of MEMS, 2010, William Andrew Publishing, Boston, USA.

[14] T. Kawase et al., “Inkjet printed via-hole interconnections and resistors for all-polymer transistor circuits”, Advanced Materials, Vol. 13, No. 21, Nov. 2001.

[15] Y. Li et al., “An all-inkjet printed flexible capacitor for wearable applications”, 2012 symposium on design, test, integration and packaging of MEMS/MOEMS, pp. 192-195, 2012.

[16] H. Minemawari et al., “Inkjet printing of single-crystal films”, Nature, Vol. 475, No. 7356, Jul. 2011.

[17] M. Mäntysalo et al, “An inkjet-deposited antenna for 2.4 GHz applications”, AEU – International Journal of Electronics and Communications, Vol. 63, No. 1, pp. 31-35, Jan. 2009.

[18] J. Miettinen et al, “Inkjet printed System-in-Package design and manufacturing”, Microelectronics Journal, Vol. 39, No. 12, pp. 1740-1750, Dec. 2008.

[19] S. Magdassi (ed.), The chemistry of inkjet inks, 2009, World Scientific Publishing Company, UK.

[20] K. Dick et al. “Size-dependent melting of silica-encapsulated gold nanoparticles”, Journal of the American Chemical Society, Vol. 124, No. 10, pp. 2312-2317, Dec. 2002.

[21] B. Ingham et al., “How nanoparticles coalesce: an in situ study of Au nanoparticle aggregation and grain growth”, Chemistry of Materials, Vol. 23. pp. 3312-3317, Jun. 2011.

[22] Harima NPS-J datasheet: nano paste series. Available: http://www.harima.co.jp/en/products/electronics/download.html, Visited: 25.09.2015.

[23] J. Z. Wang et al, “Dewetting of conducting polymer inkjet droplets on patterned surfaces”, Nature Materials, Vol. 3, pp. 171-176, Feb. 2004.

[24] D. Soltman et al, “Inkjet-printed line morphologies and temperature control of the coffee ring effect”, Langmuir, Vol. 24, No. 5, pp. 2224-2231, Jan. 2008.

[25] M. Cloupeau et al. “Electrostatic spraying of liquids in cone-jet mode”, Journal of Electrostatics, Vol. 22, No. 2, pp. 135-139, 1989.

[26] M. W. Lee et al, “Effects of pulsing frequency on characteristics of electrohydro-dynamic inkjet using micro-Al and nano-Ag particles”, Experimental Thermal and Fluid Science, Vol. 46, pp. 103-110, Apr. 2013.

[27] SIJ-S030 Technical specifications, Available: http://lasallescientific.com/wp-content/uploads/2014/06/SIJ-S030.pdf. Visited: 28.09.2015.

[28] ULVAC, Nano metal ink datasheet, Available: http://ulvac.skyworld.com/userfiles/files/Nano%20Ink/NANOMETAL_INK_CATALOG_update_2011%204%2014.pdf, Visited: 28.09.2015.

[29] ANP, Silver Jet Ink datasheet, Available: http://anapro.com/eng/product/silver_inkjet_ink.html, Visited: 28.09.2015.

[30] T. T. Allen, Introduction to engineering statistics and lean sigma: statistical quality control and design of experiments and systems, 2nd edition, 2010, Springer-Verlag, London, UK.

[31] V. Pekkanen et al., "Functional fluid jetting performance optimization", Microelectronics Reliability, Vol. 50, pp. 864-871, March 2010.

[32] J. A. Sadie et al., "Three-dimensional inkjet-printed interconnects using functional metallic nanoparticle inks", Advance Functional Materials, Vol. 24, No. 43, pp. 6834-6842, Nov. 2014.

[33] S. Enderling et al., "Sheet resistance measurement of non-standard cleanroom materials using suspended greek cross test structures", IEEE Transactions on Semiconductor Manufacturing, Vol. 19, No. 1, Feb. 2006.

[34] J. M. Choi et al., "Humidity sensor using an air capacitor", Transactions of Electrical and Electronic Materials, Vol. 14, No. 4, pp. 182-186, Aug. 2013

APPENDIX A

Humidity (%)	speed (mm/s)	vmax (V)	vbias (V)	freq (Hz)	wave-form	distance (µm)	width (µm)
55	0,45	170	245	120	triangle	70	7,8
55	0,45	180	245	100	sine	50	21,4
55	0,45	170	255	120	triangle	50	16,9
55	0,45	170	255	100	triangle	70	12
55	0,4	170	255	120	sine	50	19,8
55	0,45	170	255	120	sine	70	14,1
55	0,4	180	245	100	sine	70	16,9
55	0,45	180	245	100	triangle	70	9,9
55	0,45	180	255	120	triangle	70	12,8
55	0,45	180	255	120	sine	50	21,7
55	0,45	170	245	120	sine	50	19,4
55	0,4	170	255	120	triangle	70	12,7
55	0,45	170	255	100	sine	50	22,8
55	0,4	170	245	100	triangle	70	11,7
55	0,4	180	255	120	sine	70	17,7
55	0,45	180	255	100	triangle	50	20,4
55	0,45	170	245	100	triangle	50	16,6
55	0,4	170	245	100	sine	50	20,5
55	0,4	170	245	120	sine	70	14,2
55	0,4	180	255	100	triangle	70	15,6
55	0,4	180	245	100	triangle	50	18,4
55	0,45	170	245	100	sine	70	16,1
55	0,4	180	255	120	triangle	50	19
55	0,45	180	245	120	sine	70	14,1
55	0,45	180	255	100	sine	70	18,7
55	0,4	170	255	100	triangle	50	17,8
55	0,4	180	255	100	sine	50	22,9
55	0,4	170	245	120	triangle	50	15
55	0,4	180	245	120	triangle	70	9,7
55	0,4	170	255	100	sine	70	16,3
55	0,4	180	245	120	sine	50	18,4
55	0,45	180	245	120	triangle	50	14,6
45	0,4	170	255	120	triangle	50	15,6
45	0,45	180	245	120	sine	50	14,6
45	0,45	170	245	100	triangle	70	0
45	0,45	180	255	100	sine	50	17,4
45	0,4	170	245	120	sine	50	16,5
45	0,4	180	245	120	sine	70	14,8
45	0,45	180	245	120	triangle	70	7,1
45	0,4	180	255	120	triangle	70	9,4
45	0,4	180	255	120	sine	50	18,5
45	0,4	170	245	100	triangle	50	13,7

45	0,45	170	245	120	sine	70	9,6
45	0,45	180	245	100	sine	70	12,3
45	0,4	180	255	100	triangle	50	13,9
45	0,45	180	255	100	triangle	70	9,6
45	0,4	180	255	100	sine	70	15,1
45	0,4	180	245	100	sine	50	18,1
45	0,45	170	245	120	triangle	50	7,3
45	0,45	180	255	120	sine	70	10,3
45	0,4	180	245	120	triangle	50	8,6
45	0,45	170	255	120	sine	50	12,7
45	0,45	170	245	100	sine	50	12,8
45	0,4	170	255	100	triangle	70	6,8
45	0,4	170	255	120	sine	70	9,1
45	0,45	170	255	120	triangle	70	3,6
45	0,4	180	245	100	triangle	70	7,3
45	0,45	170	255	100	triangle	50	12,2
45	0,45	170	255	100	sine	70	12,1
45	0,4	170	255	100	sine	50	17,5
45	0,45	180	255	120	triangle	50	11,1
45	0,4	170	245	120	triangle	70	6,7
45	0,45	180	245	100	triangle	50	12,1
45	0,4	170	245	100	sine	70	11,3
55	0,4	170	255	100	sine	70	23,7
55	0,45	170	255	100	sine	50	27,9
55	0,45	170	255	100	triangle	70	19,7
55	0,45	170	255	120	sine	70	20,5
55	0,45	170	255	120	triangle	50	20,9
55	0,4	170	245	120	triangle	50	19,1
55	0,4	180	255	120	triangle	50	21,4
55	0,4	180	255	100	triangle	70	17,6
55	0,4	170	255	120	triangle	70	14,8
55	0,4	180	245	100	triangle	50	21,3
55	0,45	180	255	100	triangle	50	23
55	0,45	180	245	120	sine	70	18,1
55	0,4	180	245	120	sine	50	23,4
55	0,45	170	245	120	sine	50	21,9
55	0,4	180	245	100	sine	70	20,3
55	0,4	170	245	100	sine	50	23,8
55	0,4	180	245	120	triangle	70	12,7
55	0,45	180	255	120	sine	50	24,4
55	0,45	170	245	100	triangle	50	19,9
55	0,45	180	255	120	triangle	70	16
55	0,4	170	255	100	triangle	50	21,9
55	0,4	180	255	120	sine	70	18,7
55	0,4	170	255	120	sine	50	25,3
55	0,4	170	245	100	triangle	70	14,8

55	0,45	180	245	100	triangle	70	14,3
55	0,45	170	245	100	sine	70	18,1
55	0,4	180	255	100	sine	50	27,8
55	0,45	180	255	100	sine	70	21,4
55	0,45	170	245	120	triangle	70	10,9
55	0,4	170	245	120	sine	70	15,4
55	0,45	180	245	120	triangle	50	18,7
55	0,45	180	245	100	sine	50	23,4
45	0,45	180	245	100	triangle	50	17,5
45	0,4	180	245	120	triangle	50	15,2
45	0,4	180	255	120	triangle	70	11,6
45	0,45	180	255	120	sine	70	15,8
45	0,4	170	245	120	triangle	70	11,2
45	0,45	180	255	100	triangle	70	11,1
45	0,4	170	245	120	sine	50	19,4
45	0,4	170	245	100	sine	70	10,5
45	0,4	180	255	100	triangle	50	17,2
45	0,4	180	245	100	sine	50	18,5
45	0,4	170	245	100	triangle	50	11,7
45	0,45	170	255	120	triangle	70	6,3
45	0,45	170	255	120	sine	50	15,5
45	0,45	180	245	100	sine	70	13,1
45	0,4	170	255	100	sine	50	16,9
45	0,4	170	255	120	sine	70	10,5
45	0,4	180	245	100	triangle	70	9,2
45	0,45	180	245	120	sine	50	14,1
45	0,45	170	245	120	sine	70	9
45	0,45	180	255	120	triangle	50	13
45	0,4	170	255	100	triangle	70	10
45	0,4	170	255	120	triangle	50	11,2
45	0,45	170	245	100	triangle	70	6,6
45	0,4	180	255	120	sine	50	18,3
45	0,45	170	255	100	sine	70	12,9
45	0,4	180	245	120	sine	70	9,5
45	0,45	170	245	100	sine	50	12,7
45	0,45	180	255	100	sine	50	15,5
45	0,45	170	255	100	triangle	50	13,1
45	0,45	170	245	120	triangle	50	7,5
45	0,45	180	245	120	triangle	70	6,2
45	0,4	180	255	100	sine	70	10,4

APPENDIX B

run order	vmax (V)	vbias (V)	freq (Hz)	speed (mm/s)	distance (μm)	width (μm)
1	185	245	100	0,4	50	15
2	185	255	100	0,45	70	11,6
3	175	255	120	0,4	70	6,1
4	175	245	100	0,4	70	7,1
5	180	250	110	0,425	60	10,5
6	185	255	100	0,4	50	18,7
7	175	245	120	0,45	50	8,5
8	175	255	120	0,4	50	12,5
9	180	250	110	0,425	60	9,3
10	175	245	100	0,45	50	12,1
11	185	255	120	0,45	50	12,3
12	185	245	100	0,45	50	13,1
13	185	245	100	0,4	70	8,3
14	175	245	120	0,4	70	0
15	180	250	110	0,425	60	8,5
16	185	255	100	0,4	70	10,6
17	175	255	100	0,4	70	9,4
18	185	245	120	0,4	70	2,2
19	175	245	100	0,4	50	12,5
20	175	245	100	0,45	70	5,4
21	175	255	120	0,45	50	10,3
22	175	255	100	0,4	50	14,9
23	185	255	120	0,4	70	5,1
24	175	245	120	0,4	50	6,5
25	180	250	110	0,425	60	8,1
26	185	255	100	0,45	50	15,9
27	185	245	120	0,45	70	0
28	185	245	120	0,4	50	9,5
29	185	245	100	0,45	70	6,3
30	175	255	100	0,45	50	13,4
31	180	250	110	0,425	60	7,6
32	175	255	100	0,45	70	7,6
33	175	245	120	0,45	70	0
34	180	250	110	0,425	60	9,6
35	185	255	120	0,4	50	13,7
36	185	245	120	0,45	50	9,1
37	185	255	120	0,45	70	5
38	180	250	110	0,425	60	7,6
39	180	250	110	0,425	60	8,2
40	175	255	120	0,45	70	3,4
41	180	250	133,66	0,425	60	0
42	180	250	110	0,425	60	7,3

43	180	250	110	0,425	60	7,2
44	180	250	110	0,425	60	6,9
45	180	250	110	0,48415	60	6,9
46	180	250	110	0,36585	60	7,5
47	168,17	250	110	0,425	60	5
48	180	250	110	0,425	83,66	0
49	180	250	110	0,425	36,34	17,8
50	180	250	110	0,425	60	5,7
51	180	250	86,34	0,425	60	10,6
52	180	238,17	110	0,425	60	2,5
53	180	261,83	110	0,425	60	9,5
54	191,83	250	110	0,425	60	7,2
55	180	250	110	0,425	60	5
56	180	250	110	0,425	60	5
57	180	250	110	0,425	83,66	0
58	180	250	110	0,425	36,34	17,5
59	180	250	110	0,425	60	5,4
60	180	250	133,66	0,425	60	0
61	180	261,83	110	0,425	60	8,1
62	180	250	110	0,36585	60	4,7
63	180	250	86,34	0,425	60	9,7
64	180	250	110	0,425	60	4,5
65	168,17	250	110	0,425	60	2,6
66	180	238,17	110	0,425	60	0
67	191,83	250	110	0,425	60	5,6
68	180	250	110	0,48415	60	3,5
69	185	245	100	0,4	50	9,4
70	175	255	100	0,4	50	11,2
71	175	255	120	0,4	50	6,4
72	180	250	110	0,425	60	4,3
73	175	245	100	0,4	50	7,2
74	175	255	100	0,4	70	3,7
75	180	250	110	0,425	60	3,2
76	180	250	110	0,425	60	3,1
77	175	245	120	0,45	70	0
78	180	250	110	0,425	60	2,1
79	175	255	120	0,45	50	4,5
80	180	250	110	0,425	60	3
81	185	255	100	0,4	50	17,9
82	185	255	120	0,45	50	12,1
83	185	255	100	0,4	70	10,8
84	180	250	110	0,425	60	7,4
85	185	255	100	0,45	70	9
86	180	250	110	0,425	60	7,3
87	175	255	120	0,45	70	3,7
88	175	245	120	0,4	50	6,6

89	185	245	120	0,4	70	0
90	185	255	120	0,4	70	3,3
91	175	255	100	0,45	50	11,3
92	185	255	120	0,4	50	9,9
93	175	245	120	0,45	50	3,9
94	175	245	120	0,4	70	0
95	185	255	120	0,45	70	2,3
96	185	245	100	0,45	70	3,9
97	185	245	100	0,4	70	4,8
98	175	245	100	0,45	70	0
99	185	245	120	0,4	50	5,2
100	185	245	120	0,45	50	5,1
101	180	250	110	0,425	60	3,9
102	175	255	100	0,45	70	4,4
103	185	245	120	0,45	70	0
104	185	245	100	0,45	50	9,5
105	175	255	120	0,4	70	0
106	185	255	100	0,45	50	13,9
107	175	245	100	0,4	70	2,6
108	175	245	100	0,45	50	9,4